Physical model investigation of mid-scale mangrove effects on flow hydrodynamics and pressures and loads in the built environment

Tori Tomiczek [a,*], Anna Wargula [a], Pedro Lomónaco [b], Sabella Goodwin [a], Dan Cox [b], Andrew Kennedy [c], Pat Lynett [d]

[a] United States Naval Academy, 590 Holloway Road, Mail Stop 11D, Annapolis, MD, 21402, USA
[b] Oregon State University, 101 Kearney Hall, Corvallis, OR, 97331, USA
[c] University of Notre Dame, 168 Fitzpatrick Hall, Notre Dame, IN, 46556, USA
[d] University of Southern California, 3620 South Vermont Ave., Los Angeles, CA, 90089, USA

ABSTRACT

Large (km-scale) mangrove forests can provide protection to shorelines and near-coast structures during extreme coastal flood events, including tsunamis and tropical cyclones. However, little is known about the effects of mangroves with a modest cross-shore thickness (~10–50 m), on flow hydrodynamics and resulting inland pressures and forces on near-coast structures. We constructed a 1:16 geometric-scale physical model of a *Rhizophora mangle* (red mangrove) fringe with modest cross-shore thickness to measure the effects of a mangrove forest's cross-shore thickness on wave attenuation and subsequent load reduction on near-coast structures, idealized during experiments with an array of cubes. Three configurations, one baseline with zero mangroves and two with mangrove cross-shore thicknesses corresponding to prototype-scale forest widths of 8.2 m and 19.0 m, were considered in front of an array of idealized slab-on-grade residential buildings. Transient wave conditions with varying incident parameters (wave amplitude, wave representative time scale, water level/mangrove emergence, and presence of a background current) were considered. Water surface elevations, water velocities, cross-shore forces, and pressures measured near and against the building array indicate that mangroves affected inland flow hydrodynamics and forces. The presence of mangroves was associated with elevated water levels and reduced peak velocities between the mangroves and inland structures. Increasing the mangrove cross-shore thickness reduced the cross-shore force on a structure by 11%–65% compared to the baseline case without mangroves. The force reduction by the mangrove configurations varied with incident wave representative time scale; waves with longer representative time scales required larger cross-shore thicknesses to provide similar force reductions to those observed for shorter waves. Further investigation into a wider range of mangrove cross-shore thicknesses, trunk densities, and wave conditions is needed to inform engineering performance of natural and nature-based features for resilient coastal design.

1. Introduction

Coastal communities worldwide are threatened by both chronic (nuisance flooding, sea level rise) and acute (tropical cyclone, tsunami) flood hazards. These events disrupt transportation, power, water, and communication networks and damage buildings, including residential buildings and critical facilities, putting human lives at risk. The vulnerability of these nearshore regions is increasing, owing to higher population densities continuing to settle near the coast (Small and Nicholls, 2003) as well as climate change exacerbating the frequency

and magnitude of coastal hazards (Sweet et al., 2017; IPCC, 2013). Therefore, coastal communities across the globe require sustainable, resilient adaptation solutions to mitigate the impacts of rising seas and extreme events so that they may continue to thrive in present and future coastal environments.

As coastal communities search for adaptation solutions, an emerging body of literature has identified mangroves, wetlands, and other natural systems as effective in wave height attenuation and flood mitigation, while providing additional co-benefits such as ecosystem and cultural services (Reid et al., 2005; Farber et al., 2006; Scyphers et al., 2011,

2015). In particular, mangrove forests, located along coastlines in 118 countries and territories in tropical and subtropical areas, have been observed to mitigate waves and provide protection during tropical cyclones and tsunamis (Giri et al., 2011; Alongi, 2008; Pontee et al., 2016; Tomiczek et al., 2020). However, the protection provided to coastal infrastructure by mangrove forests in terms of a reduction in wave loading has not been quantified. This uncertainty creates challenges in the effective incorporation of natural and nature-based features into engineering design for community resilience. In addition, the performance of mangroves over various spatial scales, an important consideration in engineering design, is not well understood. Although previous studies have documented the benefits of km-scale mangrove forests (Zhang et al., 2012), little is known about benefits of mangrove forests with modest thicknesses of the mangrove belt (10–50 m) that are often found along shorelines of coastal communities.

The goal of this work is to quantify the effects of mangrove fringes with modest cross-shore thickness on inland hydrodynamic characteristics as well as the forces and pressures on near-coast infrastructure shielded by mangrove forests. This paper is structured as follows. In the remainder of Section 1, we describe characteristics of mangrove species and previous field, computational, and laboratory investigations of mangrove effects on wave transformation and propagation. Section 2 describes the scaling, laboratory setup, wave conditions, and instrumentation used in the physical model experiments for this study. Section 3 presents results indicating the effects of mangrove configurations of varying modest cross-shore thicknesses on hydrodynamic characteristics in the nearshore as well as on forces experienced by idealized structures located inland of the mangrove testing section. Section 4 discusses relationships between physical and hydrodynamic parameters and load reduction on inland structures and identifies areas for future work, and we present conclusions of this study in Section 5. The Appendix discusses the effects of mangrove configurations on pressure distributions against the idealized structures.

1.1. Characteristics of mangrove shorelines

Mangroves trees are found in subtropical and tropical coastal and brackish waters. Studies have estimated that mangrove forests comprised 140,000–150,000 km^2 worldwide at the beginning of the century (Spalding et al., 2010; Giri et al., 2011). Two-thirds of the world's mangroves are found in 12 countries, with nearly 42% of mangrove forests found in South and Southeast Asia (Spalding et al., 1997, 2010), where Indonesia, in particular, is home to the largest expanses of mangrove forests (22%) (Giri et al., 2011). Mangroves represent a diverse group of trees and shrubs, with species diversity tending to decrease with increasing latitude (Ellison, 2002). For example, the Indo-Malaysian region (~6ºS – 6ºN) represents one of the most diverse mangrove habitats worldwide, with 48 mangrove species (Duke et al., 1998), while 3 species of mangroves thrive in southern Florida of the United States (~24ºN – 27ºN): red mangroves (*Rhizophora mangle*), black mangroves (*Avicennia germinans*), and white mangroves (*Laguncularia racemosa*). The latitudinal limits of mangroves have been reported at 32ºN and 38ºS (Quisthoudt et al., 2012) and future climate change is likely to cause mangroves to spread into higher latitudes across the globe (Lovelock et al., 2019).

The *Rhizophora* genus was chosen as the focus for this study, owing to its prevalence in intertidal zones around the world. Trees in this genus are often distinguished into four groupings: *R. mangle* and *R. racemosa* in the Atlantic-East Pacific region, and *R. mucronata-stylosa* and *R. apiculata* in the IndoWest Pacific region, with several hybrid species (Duke et al., 2001). *R. mangle* thrive seaward of other mangrove species including *A. germinans*, *L. racemosa*, as well as buttonwood trees (*conocarpus erectus*). These species are found across western Africa, South America, Mexico, and the Florida Keys, while other *Rhizophora* species including *R. apiculata, R. mucronata, R. racemosa*, and *R. stylosa* may be found in concentrated or patchy local regions (Spalding et al., 2010).

Trees of the *Rhizophora* genus are characterized by their complex system of stilt roots, also called prop roots, forming dense networks extending from the trunk to the ground. Ong et al. (2004) found that 10–20% of the biomass of *R. apiculata* trees sampled in the Matang mangrove forest, Malaysia, was apportioned to these prop roots.

1.2. Previous studies of mangrove effects on nearshore hydrodynamics

Previous studies have leveraged theoretical solutions, field observations, computational simulations, and physical model experiments to investigate the effects of mangrove forests on wave transformation and inland damage mitigation. Mendez and Losada (2004) presented a widely accepted theoretical model for wave transformation over vegetation fields at various depths, which relates wave height transformation to wave characteristics, geometric and physical properties of the plants, and a drag coefficient specific for each plant. Field campaigns have shown that mangrove forests attenuate boat wakes (Trung et al., 2015; Ismail et al., 2017; Thuy et al., 2017) as well as tidal and wind-generated wave conditions (Mazda et al., 1997a; Quartel et al., 2007; Bao, 2011; Horstman et al., 2014).

Post-disaster field studies, several complemented by computational models, have documented the protective capabilities of mangroves in reducing inland tsunami (Chang et al., 2006; Alongi, 2008; Yanagisawa et al., 2009; Cheong et al., 2013) or storm (Krauss et al., 2009; Tomiczek et al., 2020) impacts. Mangroves were observed to provide significant protection from the 2004 tsunami in southeast India, Sri Lanka, and the Andaman Islands (Danielsen et al., 2005; Kathiresan and Rajendran, 2005; Chang et al., 2006; Alongi, 2008). Zhang et al. (2012) evaluated field observations and numerical results of storm surge inundation in South Florida due to Hurricane Wilma (2005) and found that while storm surge levels tended to increase seaward of the mangrove zone, the surge amplitude and inland extent were significantly decreased by the 6–30 km wide mangrove forests. Sheng and Zou (2017) conducted a numerical investigation of the role of mangroves and salt marshes in attenuating surge and waves during Hurricane Andrew (1992) in southeast Florida, finding that removing vegetation from the model increased the inundation area and volume in the area behind Biscayne Bay. Other numerical studies have shown that these coastal habitats may reduce economic loss and damage during tropical storms and hurricanes (Liu et al., 2013; Guannel et al., 2016; Narayan et al., 2016). While many previous studies considered extensive forests with cross-shore thicknesses greater than 100 m, a post-Hurricane Irma (2017) reconnaissance study in the Florida Keys by Tomiczek et al. (2020) observed that in a region with similar near-coast structural archetypes and hydrodynamic hazard intensity measures, structures fronted by 10–50 m of mangroves consistently experienced less damage when compared to damage experienced by structures fronted by other shoreline archetypes including sandy beaches, revetments, and rip-rap.

Laboratory investigations have also made strides to improve the understanding of and develop parameterizations for wave interaction with flexible and rigid vegetation (Nepf, 1999, 2004; Nepf and Vivoni, 2000; Mendez and Losada, 2004; Neumeier, 2007; Anderson and Smith, 2014; Ozeren et al., 2014; Rominger and Nepf, 2014; Smith and Anderson, 2014; Blackmar et al., 2014; Maza et al., 2015a; Wu et al., 2015a, 2015b; 2016; Lara et al., 2016). While tests on live vegetation at full scale can identify relevant processes associated with complex wave-vegetation interaction (Lara et al., 2016), mangroves and similar coastal forests are generally modelled as rigid vegetation, or parameterized mimics. Previous experiments have simplified trees as stems without roots using polyvinyl chloride (PVC) pipe, wooden dowels, or metal rods (Tanino and Nepf, 2008; Irtem et al., 2009; Huang et al., 2011; Irish et al., 2014). Results from experiments have informed numerical model validations. Maza et al. (2015b) used IHFOAM to study tsunami interaction with mangrove forests, considering wave impingement on uniform and random distributions of emergent cylinders and validating results with experimental measurements by Huang et al.

(2011). Irish et al. (2014) measured runup, flow depths, and flow velocities of tsunami inundation through a staggered array of stems representing a patchy coastal forest and found that patchy coastal forests may provide increased protection in some areas and decreased protection in others. Other tests have considered the effects patchiness of *Avicennia* mangroves on wave dissipation (Maza et al., 2016).

Several studies focused specifically on mangroves have indicated that the *Rhizophora* species' characteristic prop roots have a significant effect on wave and/or flow attenuation (Ismail et al., 2012; Hashim and Catherine, 2013; Liu et al., 2015; Zhang et al., 2015; Maza et al., 2017, 2019). These studies have parameterized the mangrove trunk-prop root system using wire roots or plastic with a similar porosity as the root system. Strusińska-Correia et al. (2013) used relationships between water depth and submerged root volume presented by Mazda et al. (1997b) to create 1:20 scale models of mangrove trunk-prop root systems with three root densities; tsunami transmission rates from solitary wave and tsunami bore experiments were reported to be 20%. Based on field measurements of mangrove prop root geometry and elasticity, Zhang et al. (2015) constructed a 1:7.5 scale model of a mangrove forest to measure mean flow velocities, Reynolds stress, and turbulent kinetic energy around prop roots. The authors reported drag coefficients consistent with those measured in field studies. Ohira et al. (2013) conducted extensive fieldwork and provided a detailed methodology for parameterizing *Rhizophora* prop root morphology. Based on the parameterization by Ohira et al. (2013), Maza et al. (2017) constructed a 1:12 scale model of a mature *Rhizophora* mangrove and measured the drag force on individual trees and water velocities around prop roots. The authors found that velocities were reduced by up to 50% and turbulent kinetic energy increased by up to five times within the root zone compared to upstream conditions. Kazemi et al. (2018) parameterized mangrove roots as a simplified array of cylinders and used particle image velocimetry (PIV) to investigate the turbulence and flow around mangrove roots. Recently, Maza et al. (2019) constructed a 1:6 scale *Rhizophora* forest and measured wave attenuation along the 26 m forest expanse during both regular and irregular wave conditions. The authors measured wave attenuation and wave-induced forces on the mangroves through the forest; results indicated that water depth, wave height, and the frontal area of the mangroves were important parameters in determining wave decay for short-period waves.

Despite these advances in the understanding of fluid-mangrove interactions, the accompanying changes to wave-induced forces and pressures on nearshore structures are not well understood. Furthermore, it is critical that engineers understand processes affecting flow through mangrove forests of modest cross-shore thickness in order to identify cross-shore thicknesses required for mangroves to produce noticeable (if any) reductions in wave heights, water velocities, and wave-induced forces and pressures on nearshore structures for a given event. Therefore, we constructed a 1:16 scale-model of a fringing *Rhizophora* mangrove trunk-prop root system fronting an idealized urban array in Oregon State University's Directional Wave Basin (DWB) and measured hydrodynamic parameters, pressures, and forces for varying incident wave conditions. Specifically, our experimental goals were to (1) observe the effects of varied mangrove cross-shore thicknesses on wave hydrodynamic propagation and transformation; (2) identify how increasing mangrove cross-shore thicknesses affect wave-induced pressures and forces on idealized inland structures; and (3) investigate relationships between mangrove cross-shore thickness, incident wave characteristics (*e.g.,* height, representative time scale) and load reduction on sheltered structures. In the next section, we describe details of the physical model, experimental setup, instrumentation, and test conditions.

2. Physical model experiments

2.1. Physical model of Rhizophora mangle

We constructed 100 specimens of the *Rhizophora* species' trunk-prop root system on a 1:16 geometric scale. Mangrove geometric parameters including prop root diameter, prop root density, trunk diameter, and elastic modulus were measured during a field campaign in Key West, FL (Tomiczek et al., 2019). These field measurements were complemented with the parameterizations presented by Ohira et al. (2013) to design scaled models of the mangroves, similar to previous studies (Zhang et al., 2015; Maza et al., 2017). As shown in Fig. 1, Ohira et al. (2013) idealized the mangrove trunk as a cylinder and presented empirical equations for calculating the height of the highest root H_{R_max}, the total number of primary prop roots N, root diameter ϕ, and the root horizontal spreading x_R based on the mangrove's diameter (girth) at breast height DBH, measured at a point 1.3 m above the ground or the upper point of the highest prop root. Informed by the equations and data presented by Ohira et al. (2013), field measurements from Key West, FL, and considerations from other studies, we used modifications to the parameterization of Ohira et al. (2013) to construct each specimen. Table 1 presents the dimensions of the scaled and full-sized mangrove considered in our experiments, and Table 2 presents the heights and horizontal spreading distances for the 11 pairs of prop roots at both model and full scale. Roots are indexed from the base of the mangrove to the highest root, with H_{R_1} corresponding to the lowest prop root elevation and $H_{R\_11} = H_{R\_max}$, corresponding to the highest elevation.

We machined each mangrove using a 1.3 cm diameter x 26.0 cm long PVC rod for the trunk. Using a rotary drill, we installed 11 holes along the trunk in a 45° spiral pattern at 1.3 cm vertical increments ranging from 2.5 cm to 15.2 cm above the base of the trunk, creating a total of 22 prop roots per mangrove. Galvanized steel wire with 2.5 mm diameter was threaded through the holes and fastened with cyanoacrylate. The scaled trunk diameter of 20.3 cm is within the ranges of values for girth at breast height from previous studies of the *Rhizophora* species in Thailand (Tamai et al., 1983), Indonesia (Kamiyama et al., 1988), Australia (Clough and Scott, 1989), and Malaysia (Ong et al., 2004) and field measurements at seven *R. mangle* sites in Key West, FL (Tomiczek et al., 2019). The model represents an idealization of the mangrove trunk-prop root system; therefore, the mangrove trunks and prop roots are assumed to be rigid, and geomorphological and bathymetric effects (*e.g.*, loose sediment capture and muddy environment) associated with mangrove systems are neglected in this study.

Mangroves occur in nature with irregularly positioned trunks and prop roots. Danielsen et al. (2005) found *Rhizophora apiculata* and *Avicennia marina* densities of 14–26 trees per 100 m^2, while restoration efforts recommend planting mangroves with 1.3–3.0 m spacing (Environmental Agency – Abu Dhabi, 2015). These results agree with analysis by Clough et al. (1999), who suggested thinning *R. apiculata* plantings to 15–20 stems per 100 m^2 for mangrove cultivation in the Mekong Delta, Vietnam. The goal of this project was to simulate similar mangrove densities while providing quantifiable numerical boundary conditions for future numerical modeling efforts. Therefore, we spaced mangroves at 0.17 m between trunks in the cross-shore $x_{spacing}$ (2.7 m spacing full scale), and 0.19 m in the alongshore $y_{spacing}$ (3.0 m full scale), resulting in a trunk density ρ_{trunk} of 43 trees per 1 m^2 (model-scale) or 17 trees per 100 m^2 (full-scale). Rows were staggered; the diagonal distance between trunks in adjacent rows was 0.195 m.

2.2. Laboratory setup

Experiments in the DWB were part of a larger experimental campaign investigating the effects of macro-roughness, debris, and partial or full shielding by seawalls, revetments, and vegetation. The DWB has plan dimensions 48.8 m by 26.5 m; within the basin, a 30 m long by 10 m wide test bathymetry representing that of an idealized
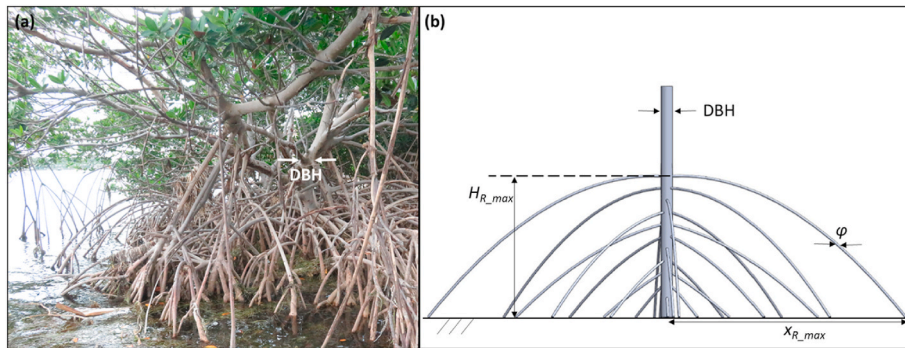
Fig. 1. (a) *R. mangle* trunk-prop root system; (b) variables defined by Ohira et al. (2013) to parameterize mangrove prop root morphology.

Table 1
Scaled and full-sized mangrove dimensions.

Dimension	Model Scale (m)	Full Scale (m)
DBH	0.013	0.203
ϕ	0.0025	0.04
H_{R_max}	0.15	2.4
x_{R_max}	0.26	4.2
$y_{spacing}$	0.19	3.0
$x_{spacing}$	0.17	2.7

Table 2
Root height and horizontal spreading.

Root Index	Model		Full	
	$H_{R,i}$ (m)	$x_{R,i}$ (m)	$H_{R,i}$ (m)	$x_{R,i}$ (m)
1	0.025	0.021	0.406	0.332
2	0.038	0.045	0.610	0.714
3	0.051	0.069	0.813	1.096
4	0.064	0.092	1.016	1.478
5	0.076	0.116	1.219	1.860
6	0.089	0.140	1.422	2.242
7	0.102	0.164	1.626	2.624
8	0.114	0.188	1.829	3.006
9	0.127	0.212	2.032	3.388
10	0.140	0.236	2.235	3.770
11	0.152	0.259	2.438	4.152

barrier island was constructed out of concrete. Upon generation, waves propagated 11.7 m over the basin's horizontal bottom before reaching a 20 m long, 1:20 concrete slope marking the onset of the test bathymetry. Guide walls were installed on either side of the concrete slope and test platform. At the crest of the slope, 100 idealized structures were installed on a 10 m long by 10 m wide horizontal platform, beyond which water dropped into a 1 m deep recirculating basin. A unique, recirculating pumping system was installed in the basin outside of the guide walls to allow the generation of conditions with waves propagating in the presence of a background current. Fig. 2 shows an oblique view of the entire basin, including the test bathymetry, guide walls, and current generation system, while plan and profile views of the test bathymetry with water depth $h = 0.98$ m can be seen in Fig. 3(a) and (b), respectively.

As shown in Fig. 2, the DWB was divided into four sections: three longitudinal sections nearest the wave maker, and one section spanning the basin width upon which the 10 m by 10 m horizontal platform with macro-roughness elements was installed 1 m above the basin floor. This section created a reservoir physically separated from the remainder of the basin by a concrete wall. The central longitudinal section, shown in Fig. 3(a) and (b), provided bathymetry leading to the horizontal platform, while rip-rap wave dissipation structures were installed in each of the longitudinal sections to the north and south of the central section to minimize effects of reflection outside the test bathymetry.

Each structure on the 10 m by 10 m horizontal platform was a cube with side length 0.40 m. Structures were installed in an idealized urban array with 1.0 m and 0.8 m spacing (center to center) in the alongshore and cross-shore directions, respectively. Eight specimens were constructed of aluminum as seen in the photographs of Fig. 3(c) and (d);
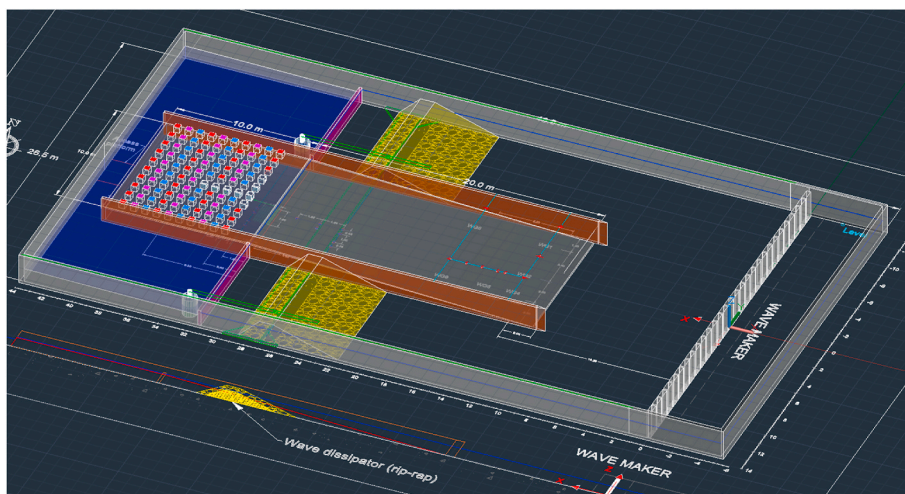

Fig. 2. Oblique view of DWB showing test bathymetry, guide walls, and recirculating pumping system.
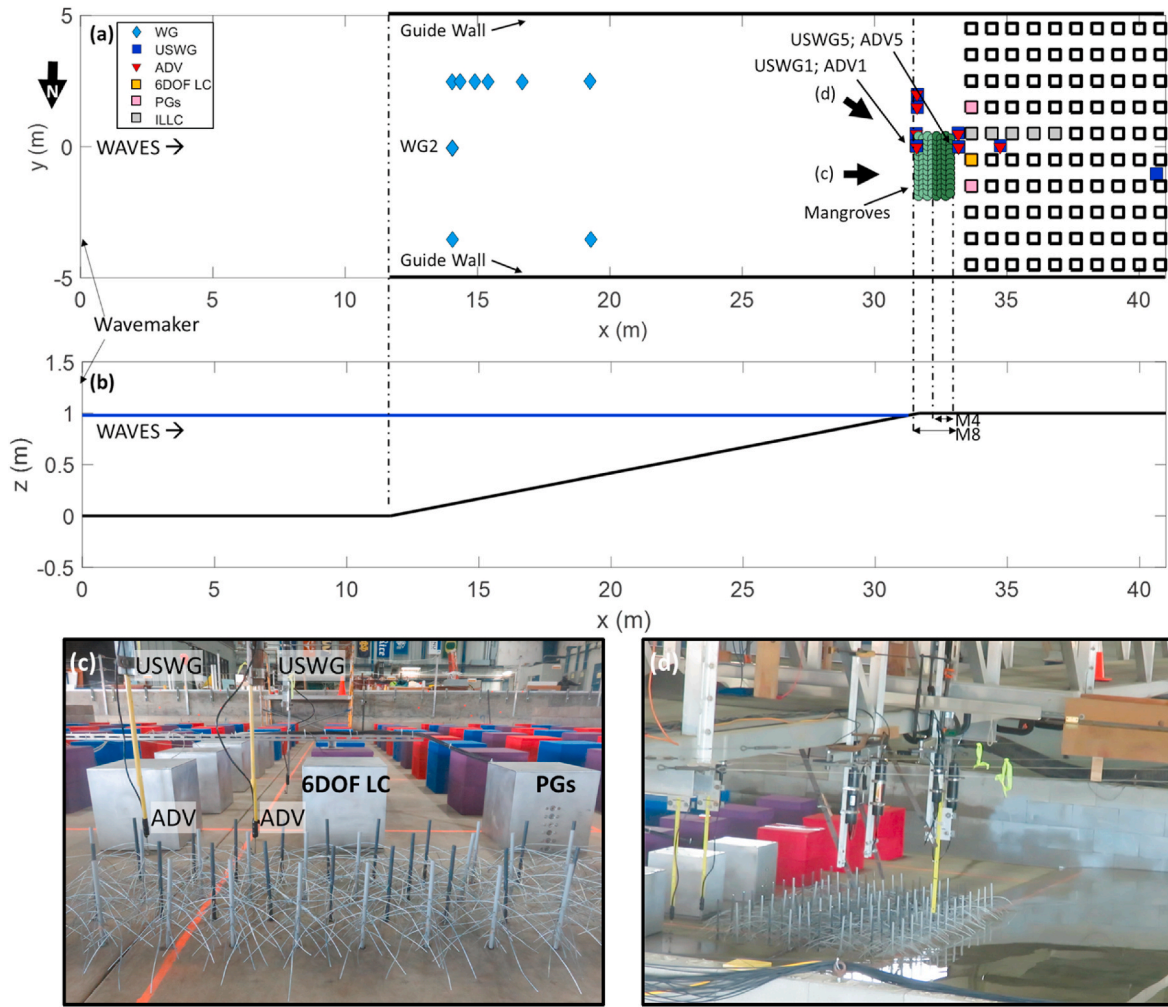
Fig. 3. (a) Plan view of mangrove configurations M4 (dark green circles only) and M8 (light green + dark green circles) fronting idealized macro-roughness specimens (array of squares). Instrumentation used for experiments are denoted as light blue diamonds (WGs), blue squares (USWGs), and red down-facing tri-angles (ADVs). Instrumented specimens are shaded gold (6DOF LC), pink (PGs), or grey (ILLCs), and uninstrumented, concrete macroroughness elements are un-shaded. Instrumentation considered in this study are labeled; (b) Profile view of basin test-section bathymetry $h = 0.98$ m; (c) Inland-looking photograph of M4 configuration and instrumentation; (d) side-looking photograph of M8 configuration, $h = 0.98$ m.

these structures were instrumented to record pressures and loads due to varied wave conditions and mangrove configurations.

This analysis investigates shielding by mangrove elements with modest cross-shore thickness and the resulting effects on inland hydro-dynamics and pressures on near-coast structures. Therefore, we focus on the three experimental configurations considering mangrove vegetation and urban macro-roughness elements: zero rows of mangroves (M0), four rows of mangroves (M4), and eight rows of mangroves (M8). Fig. 3 (c) shows an inland-facing photograph of the M4 configuration with mangroves positioned in front of idealized structural elements, and Fig. 3(d) shows a side-looking photograph of the M8 configuration during testing. The M4 configuration considered 50 mangrove models, and the M8 configuration considered an additional 50 (100 total) mangrove models installed on the horizontal platform seaward of the idealized structure array. Mangroves were secured to the concrete ba-thymetry using drop-in anchors. The two configurations with varying rows of mangroves allowed us to compare effects of varying cross-shore thicknesses of mangrove forests on inland hydrodynamic conditions and loads on the idealized structures. The cross-shore thicknesses of the three mangrove configurations were 0 m, 0.51 m, and 1.19 m (trunk to trunk) for M0, M4, and M8, respectively, representing full-scale trunk to trunk cross-shore distances of 0 m, 8.2 m, and 19.0 m, respectively. In all configurations with mangroves, the distance from the inland-most

mangrove trunk to the first row of structures in the idealized urban array was 0.41 m. For the M8 configuration, the mangrove trunks extended seaward to the intersection of the 1:20 slope with the hori-zontal test section. We note that mangrove roots extended beyond the trunks, as indicated in Table 2. The alongshore expanse of the mangrove test section was 2.3 m, or 36.5 m at full-scale, similar to the modest alongshore lengths of mangrove forests fronting structures observed in the Florida Keys by Tomiczek et al. (2020).

2.3. Instrumentation

The complete suite of instrumentation used to measure water levels, velocities, forces, and pressures during the full experimental campaign is shown in Fig. 3(a), which shows a plan view of the test section (not including pumping system exterior of the guide walls shown in Fig. 2). Water level and water velocity measurements were made offshore and onshore to characterize hydrodynamic transformation along the slope and around macro-roughness elements. Wire resistance wave gauges (WGs), ultrasonic wave gauges (USWGs), and acoustic Doppler velo-cimeters (ADVs) measured flow hydrodynamics as waves propagated across the bathymetry and in and around the mangrove and building macro-roughness elements. Six pressure gauges (PGs) were installed on an aluminum specimen shielded by mangrove configurations M4 and

M8. PGs were installed along the instrumented specimen's centerline, vertically spaced 0.04 m apart (center-to-center), with the bottommost pressure gauge installed 0.02 m above the base of the instrumented structural element. In addition to PGs, a six-degree-of-freedom load cell (6DOF LC) was installed in a structure positioned in the first row, shielded by mangrove configurations M4 and M8, and five in-line load cells (ILLCs) were positioned in the first through fifth rows as shown in Fig. 3. The x, y, and z coordinates of hydrodynamic instruments and structures housing load and pressure gauges considered in this study, and mangrove bounding locations shown in Fig. 3(a) are listed in Table 3. Cartesian coordinates are referenced with respect to the DWB coordinate system, a right–handed coordinate system where the x-axis is the cross-shore coordinate (m), positive onshore, the y-axis is the alongshore coordinate (m), with its origin at the alongshore centerline of the tank and positive to the left (south) when facing shore, and the z-axis is the vertical coordinate (m), positive upwards from the base of the basin. The photograph shown in Fig. 3(c) labels the nearshore instrumentation considered for this analysis.

For each trial, two groups of instruments were synchronized: WGs, USWGs, and ADVs recorded at 100 Hz, while PGs and load cells sampled at 1 000 Hz. All load cell and pressure data were checked for high frequency noise using a fast Fourier transform, and raw data were passed through a low pass filter of 55 Hz to account for any contribution to the signal due to background electricity. Raw and filtered measurements showed good agreement; therefore, subsequent analyses of time series and peak values considered the unfiltered data.

2.4. Wave conditions

The snake-type wave maker system in the DWB is equipped with 30 independently programmable servomotor-driven points and 29 paddles, each having a maximum stroke of 2.1 m and a board height of 2.0 m. Over the entire duration of experiments, a range of water levels and wave conditions (including solitary, transient (tsunami-like), regular, and irregular waves) were generated with and without a background current. The novel pumping system comprised two 37.3 kW (50 HP) pumps, each capable of driving 126.2 L/s (2000 gpm) of water to create a continuous background current over the test section. The flow fundamentally became stagnant and increased the water level in the basin, creating an overflow at the testing section when the water level in the basin exceeded 1 m. It took about 30 min for the system to achieve a steady state, where the volume introduced by the pumps equaled to the volume of land overflow. For the case of still water level 0.98 m, the equilibrium state was reached when the water elevation reached 1.09 m. Because the discharge was performed underwater, the current speed at the beginning of the 1:20 foreshore slope was about 0.028 m/s, considered to have minimal (Doppler and non-linear) effect on the waves during the generation stage.

The wave conditions tested for the M0, M4, and M8 configurations were scaled according to Froude similitude and included irregular and

transient waves propagating over two differing water depths depending on the presence of a background current. Here, we focus on transient waves generated using error function time series programmed into the wave maker's displacement to create long waves (e.g., Thomas and Cox, 2012). Waves were generated with or without a background current; the background current was accompanied with a 0.11 m increase in water depth to allow the pumping system to circulate water over the 10 m by 10 m horizontal test platform. This increase in water level affected the relative wave amplitude and therefore transformation of the wave signal over the bathymetry. Including a background current-only (no waves) case, seven unique trials were tested for each mangrove configuration. Fig. 4 shows the water surface elevation time series measured at WG2, located near the onset of the test section's 1:20 bathymetric slope, for the ensemble-average of each of the three wave conditions generated over mangrove configurations. Water levels were zeroed before each trial, and a 0.1 s moving average was applied to more clearly show each trial; for all trials, raw and smoothed peak amplitudes were within 10%. Dashed lines in Fig. 4 indicate trials run without a background current for ERF1 (green), ERF2 (lavender), and ERF3 (pink), with the water depth at the wave machine set to $h = 0.98$ m, while solid lines present the time series for trials run in the presence of a background current: ERF1C (green), ERF2C (lavender), and ERF3C (pink), with $h = 1.09$ m. Time series are truncated to show only the incident wave signal for which hydrodynamics and loads were considered, before a reflected wave was measured by WG2.

Table 4 shows the wave amplitude A, representative time scale T_R (defined as the duration for which the wave signal exceeded 10% of its amplitude), average cross-shore velocity u taken before the wave generation, and water depth h taken at the wave maker for each wave/current trial. The "C" suffix in the table indicates that the pumps were operating to create a background current with $h = 1.09$ m at the wave maker, while the absence of the suffix indicates that waves propagated with no background current and $h = 0.98$ m at the wave maker. Wave amplitudes and representative time scales listed in Table 4 were measured at WG2, with standard deviations of wave amplitude and representative time scale across all configurations indicated in parentheses. Wave amplitudes ranged from 0.13 to 0.22 m and varied by less than 0.02 m across configurations, while representative wave time scales ranged from 5.71 to 11.15 s and varied by 0.006–0.802 s across configurations. Greater variation in T_R was observed for trials in which

Table 3
Selected locations of instruments and specimens.

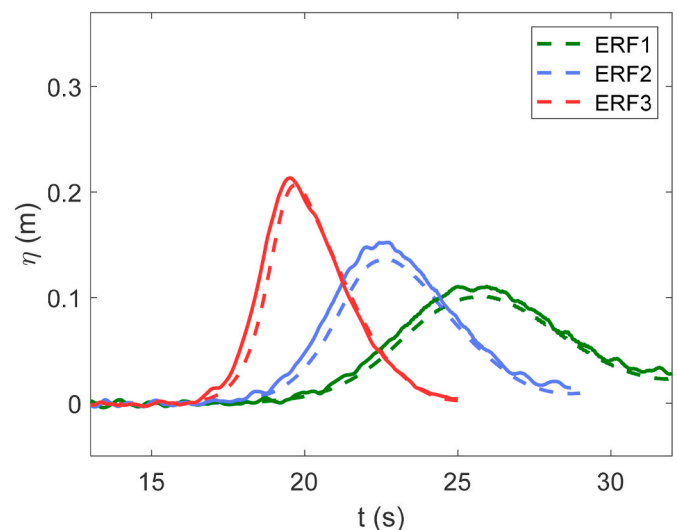| Instrument	x (m)	y (m)	z (m)
Wave maker center	0.000	0.000	0.000
WG2	14.048	−0.056	–
ADV1	31.489	−0.019	1.020
USWG5	33.170	−0.003	2.357
ADV5	33.170	−0.026	1.018
Base-center, 6DOF LC Structure	33.457	−0.503	0.993
Base-center, PG Structure	33.457	−1.503	0.993
Northwest Bound, M4, M8	32.849	−1.782	0.993
Southwest Bound, M4, M8	32.859	0.317	0.997
Northeast Bound, M4	32.340	−1.878	0.993
Southeast Bound, M4	32.341	0.403	0.995
Northeast Bound, M8	31.661	−1.878	0.989
Southeast Bound, M8	31.657	0.403	0.992

Fig. 4. Ensemble averaged water surface time series at WG2 for all transient wave trials with $h = 0.98$ m (emergent mangroves), no background current (dashed lines) and with $h = 1.09$ m (partially submerged mangroves), background current (solid lines). Line colors indicate wave condition: ERF1 (green), ERF2 (lavender), and ERF3 (pink).

Table 4

Mean (standard deviation) experimental wave conditions for M0, M4, and M8 configurations.[a]

Trial	$\overline{A}$ (m) [WG2]	$\overline{T_R}$ (s) [WG2]	u (m/s)[b] [ADV1]	h (m) [wave maker]
ERF1	0.13 (0.009)	11.15 (0.144)	0	0.98
ERF2	0.14 (0.010)	8.30 (0.006)	0	0.98
ERF3	0.21 (0.007)	5.71 (0.031)	0	0.98
ERF1C	0.14 (0.008)	10.83 (0.802)	0.31	1.09
ERF2C	0.17 (0.018)	9.20 (0.627)	0.31	1.09
ERF3C	0.22 (0.018)	5.95 (0.211)	0.31	1.09
C	0	0	0.31	1.09

[a] Location of measurement is denoted in brackets.

[b] u refers to the steady background current measured before the wave occurrence for the M0 configuration.

waves propagated in the presence of a background current ($h = 1.09$ m) and for the longest waves generated during experiments (ERF1 and ERF1C), possibly owing to small oscillations observed in Fig. 4 along the tails of these water surface elevation time series. While incident water depths at the wave maker are presented in Table 4, the two water depths considered created differing conditions at the test section. The mangrove specimens were fully emergent during trials with no background current and $h = 0.98$ m, while the specimens were partially submerged by 0.09 m (*i.e.*, the roots were 60% submerged) during trials with a background current and elevated water level of $h = 1.09$ m.

Average cross-shore velocities reported in Table 4 were measured at ADV1, located at the onset of the horizontal test section, 1.60 m seaward of the built environment. Cross-shore velocities were averaged over the first 20 s of the trials for the M0 configurations, before the transient wave reached the ADV. ADV1 measurements during the M4 and M8 configurations are not reported in Table 4. ADV1 measurements during the M4 configuration suggested offshore effects, such as reflection, by the mangroves; no ADV1 measurements were taken during the M8 configuration in order to prevent root overlap with the ADV1 instrument head. However, the consistency in velocity measurements within each mangrove configuration suggests that a similar background current was achieved for all trials.

3. Mangrove effects on hydrodynamics and inland pressures and forces

3.1. Mangrove effects on hydrodynamics

Aerial images collected using a stationary camera suspended over the wave basin suggest that the mangroves affected wave transformation, air entrainment, and resulting interaction with inland structures. Fig. 5 shows aerial images at the moment of maximum splash-up against the structures during the M4 configuration for each of the six wave conditions. For the M4 and M8 configurations, the aluminum (silver) structures were protected by mangroves while the concrete (red) structures were unshielded. The visual characteristics of the wave against the concrete structures were similar to those during the M0 configuration. The visual characteristics of the wave against the aluminum structures were similar during both the M4 and M8 configurations.

These aerial images suggest that mangroves reduced splash-up against the structures behind the mangroves during most of the wave trials. Wave breaking typically occurred either within the mangrove patch or on the idealized structures. During the M0 configuration, most wave trials interacted with the structures as broken or breaking waves, except trial ERF1C, which was nonbreaking. ERF3 initially broke just offshore of the crest of the 1:20 slope (white line, Fig. 5(c)) and impacted the first row of structures as a turbulent bore. For the M4 and M8 configurations, an aerated water surface can be seen within the mangroves (in front of the aluminum structures), alongshore of clear water in front of the concrete structures, potentially owing to mangrove-induced air entrainment. The relative reduction of splash-up against the shielded structures appears large for all wave trials conducted with $h = 0.98$ m (emergent mangroves) and no background current (Fig. 5(a), (b), and 5 (c)). For wave trials conducted with $h = 1.09$ m (partially submerged mangroves) and a trailing background current, visual wave characteristics (breaking and degree of aeration) and the relative reduction of splash-up against the structures varies between trials. The effects of mangroves on ERF1C (Fig. 5(d)) is not visually apparent; the wave did not break against the structures and the mangroves induced the least aeration in this trial. ERF2C and ERF3C (Fig. 5(e) and (f)) show minor reduction of splash-up.

Although aerial images suggest that the splash-up against the structures was reduced by the presence of mangroves (Fig. 5), the peak water level behind the mangroves in the alongshore gap between structures increased compared to the M0 configuration for all wave
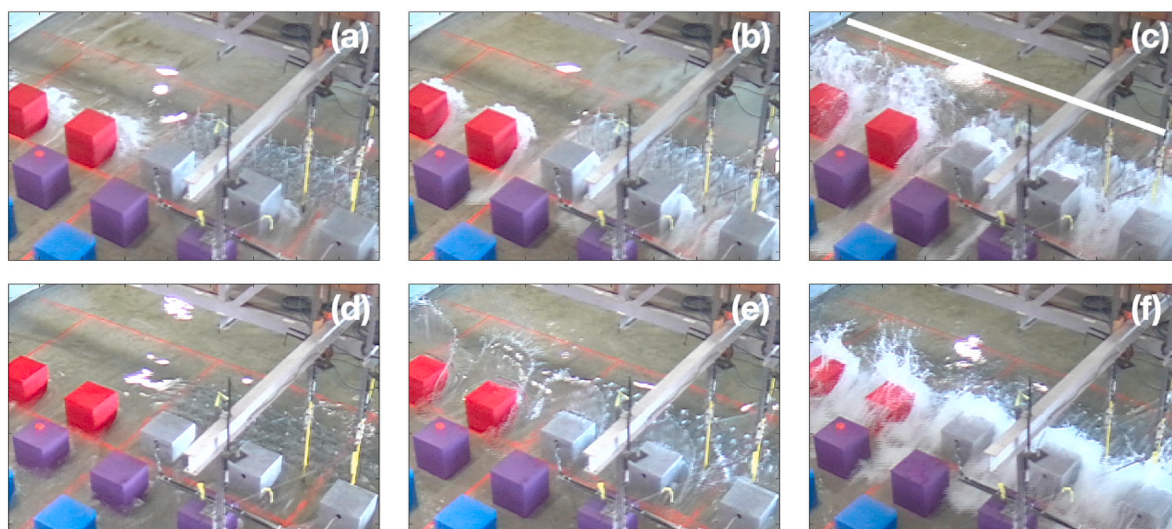

Fig. 5. Aerial images at the moment of maximum splash-up due to wave-structure interaction for transient wave cases for the M4 configuration (a) ERF1; (b) ERF2; (c) ERF3; (d) ERF1C; (e) ERF2C, and (f) ERF3C. The solid white line in panel (c) indicates the location where the wave first breaks before encountering the structures. The red line in each panel just offshore of the mangroves on the concrete bottom is the location of the crest of the 1:20 slope.

trials. Fig. 6 shows the time series of the water surface elevation η measured at USWG5 for each of the six wave conditions propagating through the M0, M4, or M8 configurations. USWG5 was zeroed at the beginning of each trial.

The percent difference, *PD,* between peak water levels smoothed with a 0.1 s running average was calculated using the following equation:

$$PD = \frac{\eta_{M0} - \eta_{MN}}{\eta_{M0}} \times (100\%) \qquad (1)$$

where η_{M0} is the peak water level for configuration M0 and η_{MN} is the peak water level for configuration M4 or M8. A positive *PD* indicates a percent reduction relative to M0; a negative *PD* indicates a percent increase relative to M0. Table 5 shows percent differences for peak water surface elevations and peak cross-shore velocities.

The increases in peak water levels relative to those in the M0 configuration during wave trials with $h = 0.98$ m (emergent mangroves) and no background current (ERF1, ERF2, and ERF3) ranged from 65 to 128%. For these wave conditions, the relative increase in peak water level was greater for wave conditions with shorter representative time scales (or larger wave amplitudes) and for shorter mangrove forest cross-shore thicknesses. During wave trials with $h = 1.09$ m (partially submerged mangroves) and a trailing background current (ERF1C, ERF2C, and ERF3C), the peak water levels relative to those in the M0 configuration increased by 24–58%. Change in peak water levels during wave trials did not show a consistent, monotonic trend with change in mangrove forest width or wave characteristics (representative time scale or amplitude). We observe an earlier arrival of the wave generated in the presence of a trailing background current ($h = 1.09$ m) compared to the same wave maker signal generated over the lower water depth and no background current. The increased water level during the trials with background current affected the relative wave amplitude and resulting shoaling characteristics as it propagated along the slope, affecting the subsequent wave-vegetation interaction. Furthermore, increasing the water level during trials with a background current reduced the frontal area of the mangroves as they interacted with the transient waves.

Peak cross-shore velocities behind the mangroves decreased compared to those in the M0 configuration for all wave trials. Fig. 7 shows time series of the cross-shore velocity measured at ADV5 for each

Table 5
Percent difference for peak water levels at USWG5 and cross-shore velocities at collocated ADV5 measured during M4 and M8 configurations compared to M0 configuration.[a]

Trial	Peak η [USWG5]			Peak u [ADV5]		
	η_{max}, M0 (m)	*PD*, M0 to M4 (%)	*PD*, M0 to M8 (%)	u_{max}, M0 (m/s)	*PD*, M0 to M4 (%)	*PD*, M0 to M8 (%)
ERF1	0.09	−83	−65	0.63	10	5
ERF2	0.11	−100	−66	2.06	68	41
ERF3	0.12	−128	−95	2.12	26	29
ERF1C	0.20	−39	−36	1.37	43	54
ERF2C	0.29	−32	−24	1.78	39	44
ERF3C	0.30	−47	−58	2.26	43	50

[a] Location of measurement is denoted in brackets.

of the six wave conditions tested. Table 5 shows the percent difference in the peak cross-shore velocity for each wave trial (Eqn. (1), replacing η with u), where the peak cross-shore velocity is defined as the maximum velocity after smoothing the time series with a 0.1 s running average. In wave trials without a background current, the lower offshore water level caused the ADV to be exposed until the arrival of the wave. The peak cross-shore velocity used in Eqn. (1) was selected after the high scatter observed in Fig. 7(a), (b), and 7(c) smoothed to a steady velocity, indicating the transition of the instrument to a good signal to noise ratio (SNR) and submerged conditions. Therefore, peak cross-shore velocities recorded may not capture velocities associated with the first arrival of the wave for these trials.

The large scatter in Fig. 7(a), (b), and 7(c) was retained to show when the wave arrived at the ADV. In these trials, the time duration of high scatter is reduced in the M4 and M8 configurations, compared to the M0 configuration. Aerial images suggest that the mangroves introduced air into the propagating wave and enhanced wave energy dissipation prior to encountering the structure, resulting in the decreased vertical jet observed in Fig. 5. The reduction in peak cross-shore velocity for ERF1 is smaller (5–10%) than that for ERF2 and ERF3 (26–68%, Table 5). This low percent difference may be owing to the lower cross-shore velocity associated with the ERF1 wave propagating through M0 configuration (less than one-third of the cross-shore velocity of ERF2 or ERF3). For the
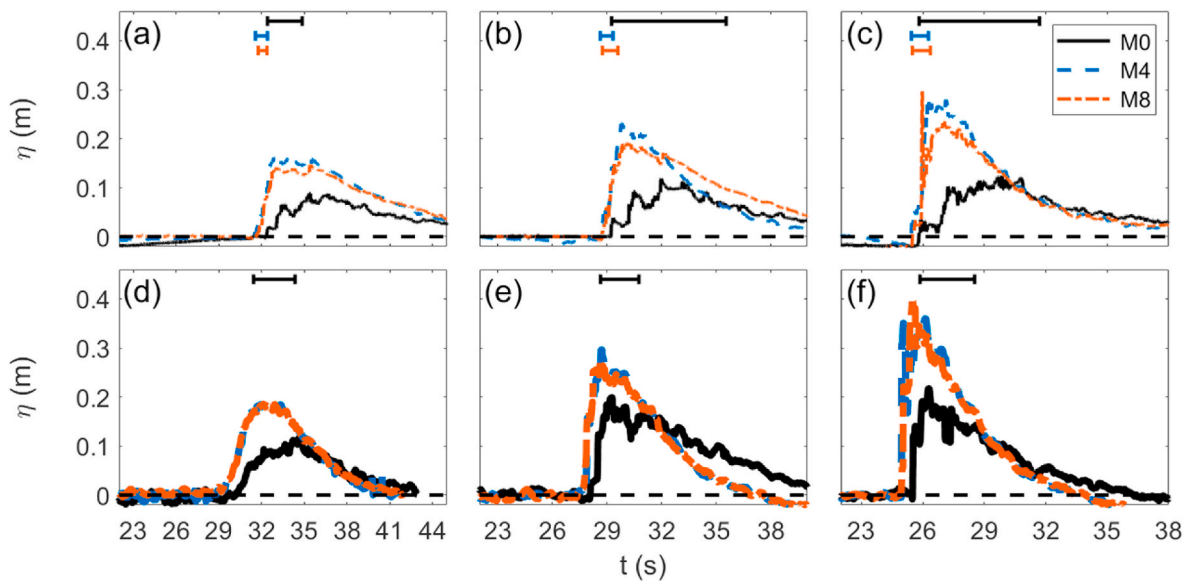

Fig. 6. Time series of water level η at USWG5 for transient wave cases (a) ERF1; (b) ERF2; (c) ERF3; (d) ERF1C; (e) ERF2C, and (f) ERF3C. Line styles indicate configuration M0 (black solid line), M4 (blue dashed line), or M8 (orange dash-dot line). Thin (a–c) and thick (d–f) lines indicate trials without background current, h = 0.98 m (emergent mangroves) and with background current, $h = 1.09$ m (partially submerged mangroves), respectively. Horizontal solid lines near the top of each panel indicate the times when ***Fr*** > 1 (calculated at co-located USWG5 and ADV5) for M0 (black), M4 (blue), and M8 (orange).
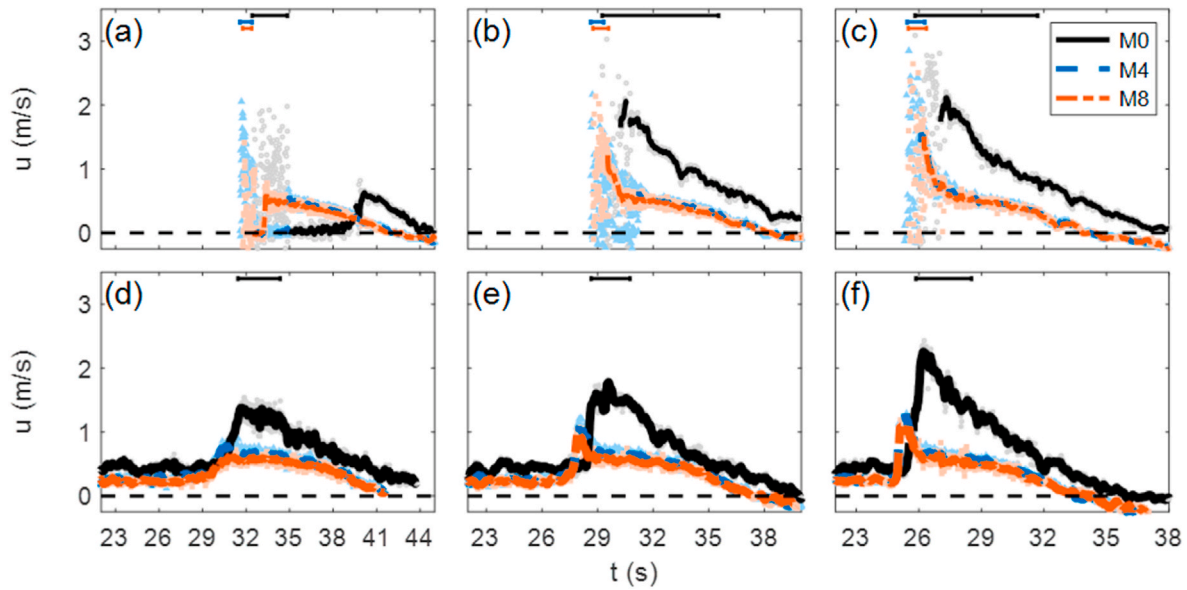
Fig. 7. Time series of cross-shore velocity u at ADV5 for transient wave cases (a) ERF1; (b) ERF2; (c) ERF3; (d) ERF1C; (e) ERF2C, and (f) ERF3C. Symbols indicate raw data and lines indicate 0.1 s averaged data. Line and marker styles indicate configuration M0 (black solid line, transparent black circles), M4 (blue dashed line, transparent blue triangles), or M8 (orange dash-dot, transparent orange squares). Thin lines and open symbols (a–c) indicate trials without background current, $h = 0.98$ m (emergent mangroves) and thick lines and filled symbols (d–f) indicate trials with background current, $h = 1.09$ m (partially submerged mangroves). Horizontal solid lines near the top of each panel indicate times when $Fr > 1$ (calculated at co-located USWG5 and ADV5) for M0 (black), M4 (blue), and M8 (orange).

ERF1 trial, we observed vertical velocities ranging from -2 to -1 m/s between the high scatter and peak cross-shore velocities, suggesting that water piled up against and deflected around the structures, converging over ADV5 in a downward rush between the structures before a strong cross-shore velocity could be established, potentially affecting peak cross-shore velocity measurements. This vertical velocity was reduced by roughly 45% in the M4 and M8 configurations, compared to that in the M0 configuration, suggesting that the mangroves induced a similar percent reduction to total velocity for wave trials ERF1, ERF2, and ERF3.

In trials ERF1C, ERF2C, ERF3C, the peak cross-shore velocity was reduced by 39–54% (Table 5), with a small increase in reduction for the larger mangrove forest width and no consistent, monotonic trend with change in wave representative time scale or amplitude. This reduction in cross-shore velocity was similar to the reduction in cross-shore velocity of the background current (measured during trial C and trials ERF1C, ERF2C, and ERF3C before the arrival of the wave). Percent reductions of the background current of 37–39% and 45–47% were observed during the M4 and M8 configurations, respectively, with no statistical difference between trials prior to the arrival of the wave. Background current velocities were consistent throughout the 20 min trial C, with a standard deviation less than 0.05 m/s for 0.1 s averaged currents, indicating that the pumps generated a uniform, steady background current across the test section for the duration of trials.

Froude numbers were calculated for all trials with collocated ADV5 and USWG5 data using:

$$Fr = \frac{U}{\sqrt{g\eta}} \tag{2}$$

where U is the total speed ($U = \sqrt{u^2 + v^2}$, with alongshore velocity v), and g is the gravitational acceleration. The horizontal bars near the top of each panel in Figs. 6 and 7 show the times when the flows were supercritical ($Fr > 1$). The presence of mangroves either reduced the time duration or eliminated supercritical flow for all wave trials. These results are similar to observations and aerial imagery from experiments, which suggested that the mangroves introduced air into waves and similarly enhanced breaking wave dissipation compared to the M0 configuration, reducing the duration of supercritical flow near the structures. We note

that the offshore initiation of the subcritical flow regime by mangroves observed for wave trials ERF1C, ERF2C, and ERF3C generated in the presence of a background current may be owing to combined effects of the trailing background current and increased offshore water depth, which allowed higher peak water levels during the M4 and M8 configurations.

3.2. Mangrove effects on inland forces and pressures

The mangrove-induced transformation of water surface elevations and cross-shore velocities for individual wave trials affected the magnitude of the wave-induced cross-shore force F_x measured by the 6DOF LC positioned behind the mangrove fringe (Fig. 3). For each configuration, the cross-shore forces measured during the current-only trial and during trials with a background current before the wave's arrival were within 8%, indicating that the background current generated by the pumps was steady. This hydrodynamic current-induced force was less than 10% of the force due to wave impingement on the structure for all trials. Therefore, we zeroed pressure gauges and load cells before the wave generation to consider the wave-induced force in all load and pressure analyses. We note that an additional dynamic contribution is associated with the waves generated in the presence of a background current owing to nonlinear interactions between waves and current and the increased water levels for trials with waves generated in the presence of a background current.

Fig. 8 shows the wave contribution to the cross-shore force F_x, normalized by $\rho g A^2 B$, where ρ is the water density and B is the alongshore width of the idealized structure, plotted against time normalized by the representative wave time scale for each of the wave trials and mangrove configurations considered during experiments. While the temporal pattern and duration of loading varied for each wave trial, the cross-shore force time series show similar trends across all configurations (M0, M4, and M8) for each unique wave trial, indicating that the mangroves subtracted energy from the flow while the waves maintained similar breaking characteristics. Experimentally generated waves with the longest representative time scales (ERF1 and ERF1C) created a quasistatic load condition on the structure, while waves with shorter representative time scales, especially ERF3C, induced peakier forces
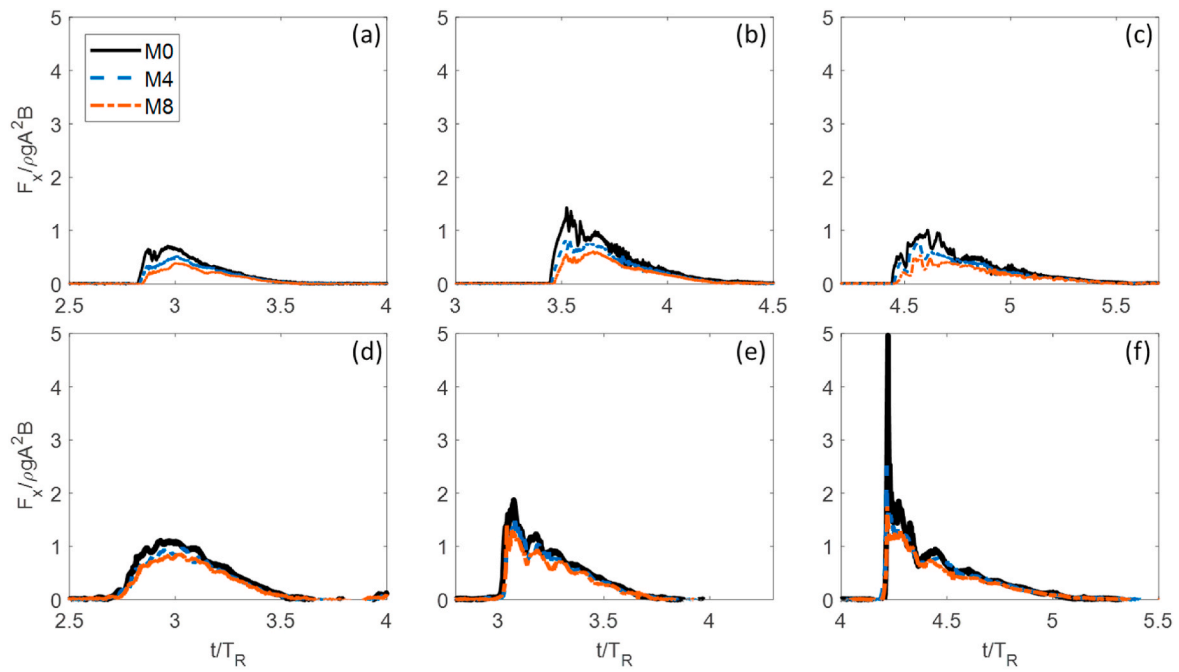
Fig. 8. Normalized wave-induced $F_x/\rho g A^2 B$ vs. t/T_R for transient wave cases with $h = 0.98$ m (emergent mangroves) over still water (a) ERF1; (b) ERF2; (c) ERF3; and $h = 1.09$ m (partially submerged mangroves) with trailing background current, (d) ERF1C; (e) ERF2C, and (f) ERF3C, based on 6DOF LC measurements. Line styles indicate configuration M0 (black solid line), M4 (blue dashed line), or M8 (orange dash-dot line).

associated with the impingement of the breaking or broken wave on the idealized structure. The time series shown in ERF3C indicates a short-duration, impulsive peak force due to the wave's initial impact on the structure, consistent with observations of breaking wave impacts by previous studies (Oumeraci et al., 1993; Cooker and Peregrine, 1995; Wood et al., 2000; Peregrine, 2003; Bullock et al., 2007; Bradner et al., 2009; Thomas and Cox, 2012; Tomiczek et al., 2016; Park et al., 2017). Although the time series show similar temporal patterns, the magnitude of the peak measured force decreased from the M0 to M4 to M8 configurations for all wave trials. This reduction was especially evident for the impulsive force induced by perfect-breaking wave of trial ERF3C in the M0 configuration.

While the cross-shore force time series shown in Fig. 8 allow for qualitative comparisons of the temporal pattern and magnitude of cross-shore forces, Fig. 9 shows the changes in the maximum cross-shore force measured by the 6DOF LC due to varying incident wave parameters or shielding by mangroves. The relationship between F_x and T_R is shown in Fig. 9(a) for all wave trials and mangrove configurations, with symbol types and colors indicating mangrove configurations M0 (black circles),

M4 (blue triangles), and M8 (orange squares); shaded symbols indicate trials generated with $h = 1.09$ m (partially submerged mangroves) in the presence of a trailing background current, and hollow symbols indicate trials generated with $h = 0.98$ m (emergent mangroves) over still water. As shown in the figure, increasing T_R was associated with decreasing F_x for all configurations; we note that waves with longer representative time scales had smaller amplitudes in this experiment. Similarly, Fig. 9 (a) indicates the effect of the presence of four or eight rows of mangroves on the total cross-shore force: for all wave conditions tested, the cross-shore forces measured during the M4 and M8 configurations were less than those measured for the M0 configuration. Effects are most readily observed for trial ERF3C ($h = 1.09$ m, $A = 0.22$ m, $T_R = 5.71$ s), which induced the largest force on the structure during the baseline M0 configuration.

Fig. 9(b) shows the measured cross-shore force F_x plotted against the cross-shore thickness of shielding mangrove configurations. Symbol types and colors indicate the varying wave maker signals for wave generation ERF1/1C (green, right-facing triangles), ERF2/2C (lavender, left-facing triangles), and ERF3/3C (pink diamonds); filled symbols
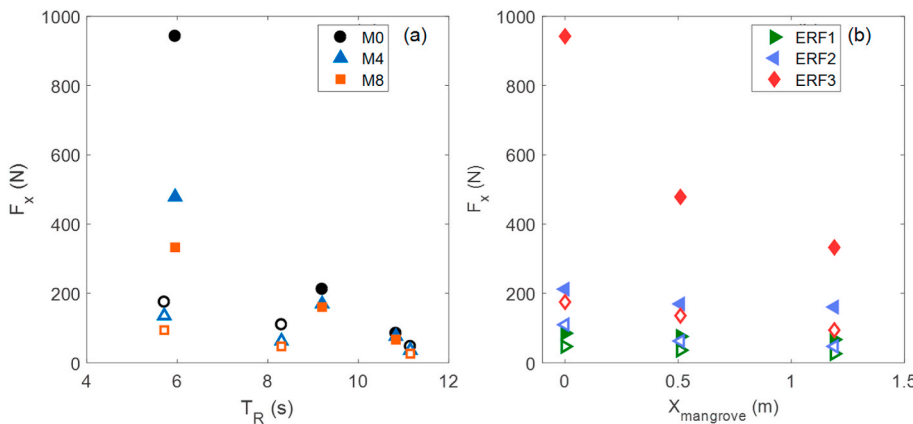

Fig. 9. Summary of peak force F_x vs. (a) representative time scale T_R for M0 (black circles), M4 (blue up-facing triangles), and M8 (orange squares) configurations, and (b) mangrove cross-shore thickness $X_{mangrove}$ for ERF1 (green, right-facing triangles), ERF2 (lavender, left-facing triangles), and ERF3 (pink diamonds) wave trials. Filled symbols: wave propagated with $h = 1.09$ m (partially submerged mangroves) and a trailing background current; hollow symbols: wave propagated with $h = 0.98$ m (emergent mangroves) over still water.

indicate waves generated at an elevated water level over a trailing background current, while hollow symbols indicate wave trials generated at the lower water level over still water. For a given mangrove configuration, waves with larger amplitudes (shorter time scales) propagating over elevated water levels in the presence of a background current tended to increase the cross-shore force measured by the 6DOF LC. Increasing the cross-shore thickness of the mangrove forest reduced the cross-shore force on the idealized structure. This reduction is most readily observed for ERF3C, which induced the largest load on the structure during the M0 configuration. The relative importance of representative time scale and amplitude to the reduction of cross-shore force is discussed further in Section 4.

The percent differences in cross-shore force calculated using Eqn. (1), substituting F_x for η, are listed in Table 6 for each wave trial and mangrove configuration. The reduction in cross-shore force was between 11 and 49% for the M4 configuration and 21–65% for the M8 configuration. For wave conditions during which waves propagated with $h = 0.98$ m (emergent mangroves) and no background current, the percent reduction was greatest for the ERF2 condition for both the M4 and M8 configurations, with ERF1 (longer representative time scale; smaller amplitude) and ERF3 (shorter representative time scale; larger amplitude) associated with a smaller PD compared to the M0 configuration. We hypothesize that wave breaking condition associated with each trial was an important contributor to wave load reduction; Fig. 5 indicates that the ERF3 wave broke just offshore of the horizontal test section during the M0 condition, allowing for wave dissipation as the broken wave propagated across the horizontal section before interacting with the structure. In contrast, the waves generated in by the ERF1 and ERF2 conditions interacted with the vegetation as breaking waves. Therefore, for similar wave breaking conditions at the location of the instrumented specimen, the percent reduction in measured force was greater for the shorter-time scale wave (ERF2). For trials run with $h = 1.09$ m (partially submerged mangroves) and in the presence of a trailing background current, the percent reduction in total force tended to increase with decreasing wave representative time scale (increasing wave amplitude).

The largest percent reductions were observed for the ERF2 and ERF3C wave trials: compared to the baseline M0 configuration, 0.51 m of mangrove shielding (M4) resulted in 43% and 49% F_x reductions and 1.19 m of mangrove shielding (M8) resulted in 57% and 65% F_x reductions, respectively. While increasing the mangrove cross-shore thickness from M4 to M8 showed a nearly linear trend in percent reduction for the ERF1, ERF3, and ERF1C trials, the additional benefit from the M4 to M8 configurations was less than the initial benefit from introducing mangroves (M0 to M4) for the ERF2, ERF2C, and ERF3C trials.

Results shown in Fig. 9 and Table 6 suggest that (1) the presence of mangroves provided measurable protection to inland structures for all wave trials considered here; and (2) the percent difference in F_x for a given wave condition (compared to a no-mangrove configuration) varied depending on physical parameters of the mangrove forest (cross-shore thickness and emergent frontal area) and incident hydrodynamic conditions (water depth, wave representative time scale and wave

amplitude). Relationships between these parameters are explored in more detail in Section 4.

While the wave-induced force on a structure is important to assess global stability of a structure and the required capacity for components, the distribution of wave-induced pressures on a structure may also be important when considering impulsive wave forces or localized damage. We compared the vertical distribution of pressures induced by each wave trial at the time of the maximum force (calculated by integrating the pressure distribution time series over the face of the idealized structure) for the three mangrove configurations (see Appendix). Results indicate that the presence of mangroves changed the shape of the pressure distribution, particularly for wave trials generated with $h = 0.98$ m (emergent mangroves) over still water. Additional tests are required to resolve more finely the spatial distribution of pressures and account for the inherent variability in impulsive wave pressure measurements (Witte, 1988; Oumeraci et al., 1993; Hattori et al., 1994).

4. Discussion

4.1. Cross-shore forest thickness effects on force reduction

Measurements showed that, for all wave conditions tested, the presence of mangroves, even at modest cross-shore thicknesses, affect flow hydrodynamics, reducing cross-shore forces on inland structures. The degree of force reduction depends on a complex relationship between the wave characteristics (*e.g.,* water depth, wave amplitude, representative time scale, breaking), the presence of a background current, and mangrove physical parameters (cross-shore thickness, emergent frontal area). We investigated the relative importance of mangrove cross-shore thickness and incident wave parameters in effecting a given percent reduction in cross-shore force compared to that force induced by waves interacting with an unshielded structure.

Fig. 10 shows the relationship between the percent difference PD in cross-shore force measured by the 6DOF LC and the cross-shore thickness of the mangroves $X_{mangrove}$ normalized by the incident wave's representative time scale, T_R, and shallow-water celerity, $\sqrt{gh}$. Fig. 10 indicates that the wave representative time scale affects the additional
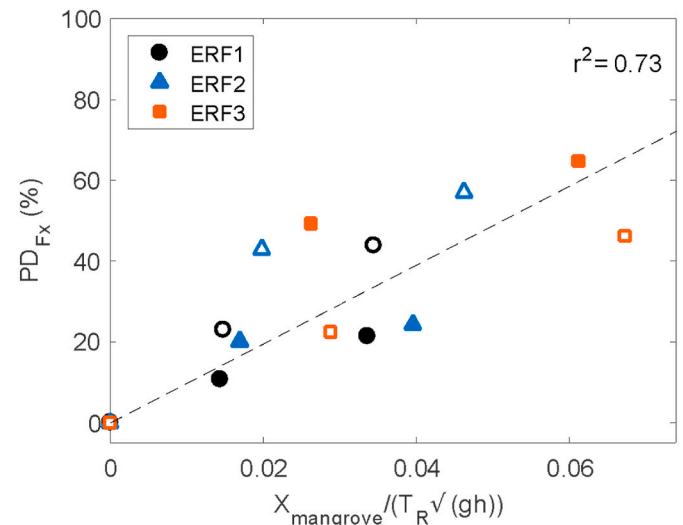

Fig. 10. Percent difference in cross-shore force measured by the 6DOF LC PD_{FX} (%) vs. mangrove cross-shore thickness $X_{mangrove}$, normalized by the incident wave representative time scale (T_R) and offshore celerity $\sqrt{gh}$. Symbols indicate incident wave conditions: ERF1 (black circles), ERF2 (blue triangles), and ERF3 (orange squares) trials. Filled symbols: wave propagated with $h = 1.09$ m (emergent mangroves) over a trailing background current; hollow symbols: wave propagated with $h = 0.98$ m (partially submerged mangroves) over still water.

Table 6
Measured cross-shore force for baseline (M0) configuration and percent reduction for M4 and M8 configurations.

Trial	Peak F_x [6DOF LC]		
	F_{xmax}, M0 (N)	PD, M0 to M4 (%)	PD, M0 to M8 (%)
ERF1	47.1	23	44
ERF2	110.0	43	57
ERF3	174.9	22	46
ERF1C	85.1	11	21
ERF2C	212.1	20	24
ERF3C	942.7	49	65

benefit associated with added mangrove cross-shore thickness. The data collapse to an approximately linear relationship between *PD* and $X_{mangrove}/(T_R\sqrt{gh})$ ($r^2 = 0.73$). Therefore, waves with longer representative time scales propagating in deeper water require larger expanses of mangrove cross-shore thicknesses to achieve the same reduction in cross-shore force. However, it should also be noted that a cross-shore thickness of mangroves that is 2–7% of the quantity $(T_R\sqrt{gh})$ had a significant effect on inland loads for the wave conditions tested here (11–65% reduction, Table 6), emphasizing the potentially significant contribution that mangroves with modest cross-shore thickness can have in providing protection from surge and tsunamis.

4.2. Other factors affecting force reduction

Wave trials considered in these experiments varied incident wave amplitude with representative time scale (Table 4), and the presence of a background current was accompanied by an increase in water level that partially submerged the mangrove configurations. Thus, the trend in Fig. 10 may also suggest effects of changing wave amplitude or wave height to water depth ratio and emergent frontal area of mangrove roots on the overall load reduction. For these trials, individual contributions of increased water level, amplitude, representative time scale, and presence of a background current cannot be separated. However, analysis of force reduction relationships between the cross-shore thickness of mangroves and incident wave amplitude ($X_{mangrove}/A$), onshore water surface elevation ($X_{mangrove}/\eta$), and root height and relative wave amplitude (($X_{mangrove}/H_{R\_max})/(A/h)$) yielded lower correlations ($r^2 = 0.46$, 0.40, and 0.44 respectively). Examination of force reduction versus mangrove cross-shore thickness normalized by $T_R\sqrt{gh}$ multiplied by relative wave amplitude ($T_R\sqrt{gh}\,(A/h)$) did not change the correlation ($r^2 = 0.73$), suggesting that the impact of wave amplitude or wave amplitude to water depth ratio may be secondary to the representative time scale of the wave.

The increase in water level from trials without a background current to those run in the presence of a trailing current changed the condition of the mangrove specimens from emergent ($h=0.98$ m, 0% submerged roots) to partially submerged by 0.09 m ($h=1.09$ m, 60% submerged roots). Experiments by Maza et al. (2019) suggest that the frontal area of mangroves associated with different water depths is a dominant variable driving wave attenuation. Partially submerging the mangrove specimens reduced the emergent frontal area of the mangrove trunk-prop root system, which affected the blockage potential during wave-vegetation interaction and resulting wave dissipation and aeration as the wave propagated through the forest.

The wave breaking condition is also an important factor in wave-vegetation interaction and the resulting impulsive and/or quasi-static loads on near-coast structures. ERF3 was the only wave trial in which the wave broke offshore of the mangroves for all configurations. The mangroves enhanced energy dissipation and further aerated the broken wave, leading to a force reduction against the structures. ERF3C had the highest force reduction of all trials, including ERF3, potentially owing to the additional effect that the mangroves had in reducing the impulsive force on the structure. In ERF3C, aerial images show that the wave begins to break just in front of the structure for the M0 configuration, inducing the impulsive force observed in Fig. 8(f). The introduction of macro-roughness (mangroves) in the M4 and M8 configurations caused the wave to lose energy within the mangroves. Work done on the mangrove elements by the wave dissipated the wave's energy before it interacted with the structure, resulting in a lower measured impact force. The additional water depth for trials ERF1C, ERF2C, and ERF3C also changed the relative wave amplitude and shoaling characteristics over the bathymetry, affecting the interaction of the wave with the mangroves. A wider range of water depths, wave representative time scales (periods), wave amplitudes, background currents, and vegetation emergence must be tested to envelope a broader range of prototype-scale conditions allowing for the identification of controlling hydrodynamic parameters and quantification of the combined effects that these parameters have on the force reduction.

4.3. Experimental considerations and areas for future work

Further work is needed to determine the effects of mangroves on inland loads and hydrodynamic transformation for other wave conditions including repeated, shorter-period waves (*i.e.*, storm waves), in order to evaluate benefits of these natural systems during daily conditions and tropical storms. Work is ongoing to analyze the transformation of irregular waves through the mangrove configurations described here; future work may further consider regular, irregular, and other wave conditions. In addition, it is critical in future tests to quantify not only the engineering benefits of mangroves but also breakpoints, or conditions at which the system is expected to fail (*i.e.*, the mangroves are damaged beyond recovery) due to either long-lasting or extreme conditions. Metrics that combine the coastal protection benefits that mangroves supply with their failure limits will be important for decision-makers to identify viable and sustainable nature-based engineering solutions.

While this study focused on the inland benefits provided by mangroves, edge and seaward effects must also be examined in future studies. Due to the alongshore gap created by the mangrove configurations in these experiments (replicating observations from fringing mangroves in Key West, FL by Tomiczek et al. (2020)), edge effects will have affected wave transformation and dissipation around the mangrove sections, potentially providing enhanced flow velocities and loads on unshielded structures located next to the mangrove patch. In addition, the presence of mangroves and structures induces wave-reflection, leading to feedbacks with inland wave propagation as well as seaward effects that may be more fully explored in future tests.

Although the wave conditions presented here represent long waves; there are still significant differences in time scales when scaling laboratory conditions to those of a tsunami (Madsen, 2008). Several alternative methods of long wave generation have been investigated, including by pneumatic wave maker (Rossetto et al., 2011), pump-driven wave maker (Goseberg et al., 2013; Bremm et al., 2015), and other systems (Synolakis, 1990; Tomiczek et al., 2016; Prasetyo et al., 2019). Experiments considering alternative long wave generation methods will further improve the understanding of interactions between mangroves of varied cross-shore thicknesses and short- and long-period waves.

In addition, scaling effects must be considered when applying experimental results to prototype conditions. The mangrove models in these tests were constructed at a 1:16 geometric scale. We checked that the Reynolds Number was sufficiently large to ensure that viscous effects did not dominate inertial effects typical of overland flow conditions at full-scale. For these trials, peak water velocities ranged from 0.63 to 2.27 m/s. The Reynolds Number ***Re*** of flow around mangrove roots, defined as ***Re*** $= ud_{root}/\nu$, where ν is the kinematic viscosity of water, ranged from 1570 to 5650, sufficient to generate turbulent wakes (Maza et al., 2017). Future work may characterize turbulence of flow around individual roots and systems of roots at larger scales and other flow velocities. Tests at a range of geometric scales will allow for identification and resolution of scale effects from model to prototype as well as the incorporation of other mechanical properties of mangroves such as elasticity.

In addition to expanding the range of wave conditions and geometric scales tested, a wider range of mangrove configurations and species must be tested in future work. Mangroves grow in nature at irregular locations and at varying tree densities. The mangrove configurations tested in these experiments correspond to a densely vegetated mangrove forest (Danielsen et al., 2005); field studies have documented a range of tree density, basal area, and *DBH* (Jin Eong et al., 1995; Dawes et al., 1999; Novitzky, 2010; Sreelekshmi et al., 2018). Future tests may

consider randomizing mangrove placement during laboratory setup to identify benefits of sparser or denser mangrove spacing than those considered in these trials. Similar to previous studies (Maza et al., 2017, 2019), this work idealizes the mangrove trunk-prop root system by neglecting effects of branches or tree canopies. However, as water levels increase, wave and current interaction with a mangrove canopy may become more important, particularly at the leading edge of a mangrove forest. Therefore, future work may seek to quantify the effect of mangrove canopies on wave propagation and transformation during extreme flooding or storm surge conditions. Further, mangroves trap sediment, effecting local bathymetric changes that affect wave transformation; this bathymetric change may similarly cause wave shoaling, breaking, and energy dissipation, but its impact has not been quantified in this study. The effects of mangrove ground rooting on anchoring trees and stabilizing local bathymetry must also be considered when evaluating the performance of these natural systems. Finally, the interaction of mangroves with other natural or hardened systems must be considered in future work when considering hybrid and multi-tiered approaches to coastal hazard mitigation. Multi-disciplinary work can further identify co-benefits of these natural and hybrid systems in terms of engineering performance, ecosystem services, and carbon storage, among others, to more holistically quantify benefits and costs associated with mangrove shorelines.

5. Conclusions

These experiments investigated effects of mangrove trunk-prop root systems with modest cross-shore thicknesses on flow hydrodynamics, and novel measurements of pressures and forces on idealized inland structures under transient wave conditions. Based on results presented above, we present the following main conclusions:

- The presence of mangroves affected inland hydrodynamic characteristics including inland water surface elevations and peak cross-shore velocities, with the M4 and M8 configurations increasing water surface elevations by 24–128% and decreasing peak cross-shore velocities by 5–68% for individual wave conditions, compared to the M0 baseline configuration. The increase in water level behind the mangroves was likely affected by wave reflection between the mangroves and building elements and wave interaction with the vegetation.
- The emergent macro-roughness associated with the mangrove configurations enhanced energy dissipation as waves performed work on mangrove elements and introduced air into the propagating wave. This wave-mangrove interaction reduced or eliminated supercritical flow behind the mangroves, similarly reducing the vertical jet associated with wave interaction with the first row of idealized structures.
- The presence of mangroves reduced the magnitude of the cross-shore wave-induced force, compared to the M0 baseline configuration, by 11–65%. The increased benefit from additional mangrove cross-shore thickness varied for unique wave conditions (water depth/ mangrove emergence, wave amplitude, wave representative time scale, and presence of a background current).
- Incident hydrodynamic conditions, including the presence of a background current, water depth, wave amplitude, and representative time scale as well as the emergence of the prop roots affected the degree of benefit due to a mangrove fringe with a given cross-shore thickness. The percent difference between the force measured for a given configuration with mangroves (M4 or M8) and the unshielded configuration (M0) varied approximately linearly with mangrove cross-shore thickness normalized by the incident wave representative time scale and offshore celerity. Longer waves required a greater cross-shore thickness for the same percent reduction in force. However, the M4 and M8 mangrove configurations reduced the cross-shore force on the 6DOF LC in all wave trials tested, despite

comprising only 2–7% of the quantity $T_R\sqrt{gh}$. Therefore, results indicate that for the range of water depths, wave amplitudes, and wave representative time scales considered in these experiments, even modest cross-shore thicknesses of the mangrove forest provided some degree of protection during overland flow conditions.

Mangroves and other natural and nature-based features offer potential as sustainable, resilient natural infrastructure that, when implemented appropriately, may provide benefits including coastal protection, habitat creation, carbon-storage, and others. While additional work is needed to fully understand the potential and limitations of mangrove forests in providing protection to inland structures, coastal communities may leverage these natural systems in suitable locations and as part of multi-tiered approaches including both natural and engineered infrastructure. Hybrid systems in which natural infrastructure can complement the performance of engineered structures (*e.g.,* seawalls, revetments) may improve the robustness and resiliency of coastal communities worldwide.

CRediT authorship contribution statement

Tori Tomiczek: Methodology, Validation, Formal analysis, Investigation, Data curation, Writing - original draft, Writing - review & editing, Visualization, Supervision, Funding acquisition. **Anna Wargula:** Methodology, Formal analysis, Writing - original draft, Writing - review & editing, Visualization. **Pedro Lomónaco:** Methodology, Validation, Investigation, Writing - review & editing, Visualization, Supervision, Funding acquisition. **Sabella Goodwin:** Methodology, Investigation. **Dan Cox:** Methodology, Writing - review & editing, Supervision, Funding acquisition. **Andrew Kennedy:** Methodology, Writing - review & editing, Supervision, Funding acquisition. **Pat Lynett:** Methodology, Writing - review & editing, Supervision, Funding acquisition.

Declaration of competing interest

The authors declare that they have no known competing financial interests or personal relationships that could have appeared to influence the work reported in this paper.

Appendix. Mangrove Effects on Dynamic Pressures on Inland Structures

We analyzed the pressure distributions over the vertical face of the specimen instrumented with PGs 1–6 during the unshielded configuration (M0) and shielded configurations M4 and M8. Fig. A1 shows the pressures at PGs 1–6 plotted along the x-axis at their respective elevations (y-axis) for each of the trials conducted with $h = 0.98$ m (emergent mangroves) and no background current. The pressure distributions shown were taken at the time of the maximum force calculated by integrating the pressure gauge measurements over the face of the structure. Similarly, Fig. A2 shows the comparison of shielded pressures to the M0 configuration for trials conducted with $h = 1.09$ m (partially submerged mangroves) and in the presence of a background current.
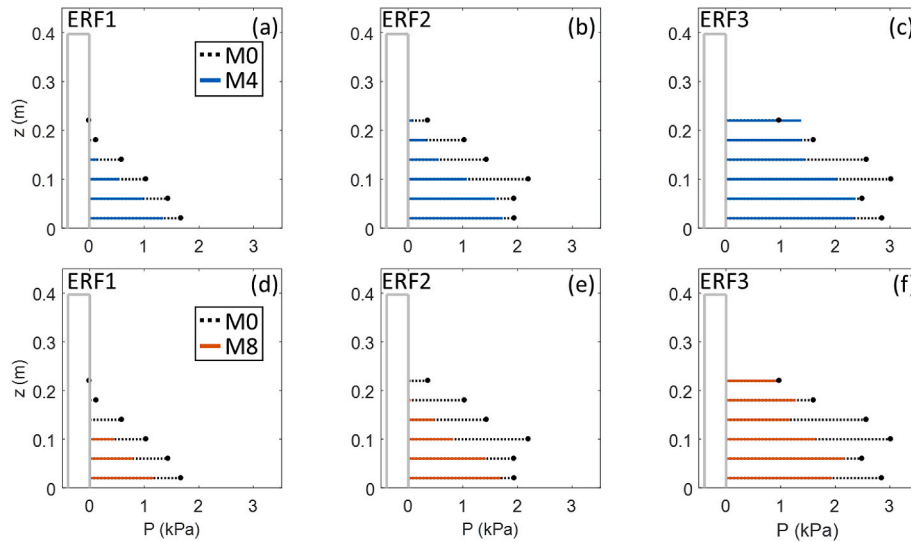

Fig. A.1. Summary of pressure distribution at the time of the peak integrated force for wave trials with $h = 0.98$ m, (emergent mangroves) over still water: (a, d) ERF1; (b, e) ERF2, and (c, f) ERF3 during (a, b, c) M4 (blue lines) configuration and (d, e, f) M8 (orange lines) configuration. Black dotted lines and circles correspond to pressure distribution at time of peak integrated force for M0 configuration.

As shown in Fig. A1, the presence of mangroves significantly changed the shape of the pressure distribution compared to the baseline M0 configuration for all three wave trials with $h = 0.98$ m (emergent mangroves) and no background current. The maximum elevation at which pressure is measured decreases from the M0 to M4 to M8 configuration for trials ERF1 and ERF2, and nearly all pressure gauges show a reduction in pressure at their respective elevation compared to the baseline M0 configuration. The elevation of the peak pressure shifts downward from PG3 (0.10 m above the base of the specimen) to PG1 (0.02 m above the base of the specimen) for ERF2 and from PG3 to PG2 for ERF3. We note that for ERF3, the highest pressure gauge (PG6, 0.22 m above the base of the structure) recorded a larger pressure in the M4 configuration and similar pressure in the M8 configuration to that measured during the baseline M0 configuration. While reduction was observed for nearly all locations on the instrumented specimen, the pressures associated with breaking or broken-wave impact can be highly variable depending on the shape of and air entrainment in the incident wave (Chen and Melville, 1988; Cooker and Peregrine, 1995; Peregrine, 2003; Bullock et al., 2007). Therefore, although mangroves were shown in Figs. 8 and 9 (see manuscript) to reduce the total force on the structure, they may not necessarily guarantee that all pressures are reduced over the vertical domain of a structure.
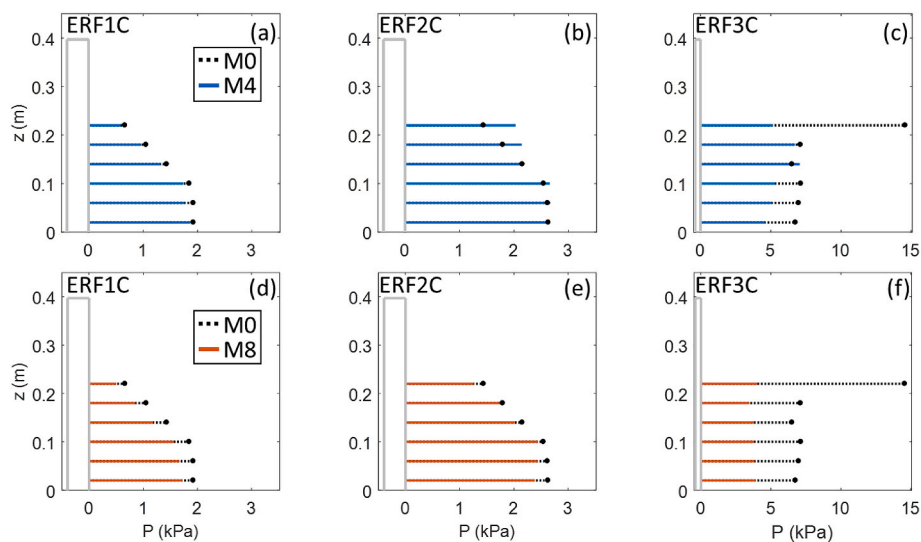

Fig. A.2. Summary of pressure distribution at the time of the peak integrated force for wave trials with $h = 1.09$ m (partially submerged mangroves), in the presence of a background current: (a, d) ERF1C; (b, e) ERF2C, and (c, f) ERF3C during (a, b, c) M4 (blue lines) configuration and (d, e, f) M8 (orange lines) configuration. Black

dotted lines and circles correspond to pressure distribution at time of peak integrated force for M0 configuration.

While Fig. A1 shows a clear reduction in peak pressures measured during shielded conditions, the effect of mangroves on pressures due to waves propagating with $h = 1.09$ m (partially submerged mangroves) and in the presence of a trailing background current (Fig. A2) is less apparent, particularly for the longer waves of ERF1C and ERF2C. Pressure gauges recorded the largest pressures at the highest elevations of pressure gauges for the M4 configuration for wave trial ERF2C, which may be related to the onshore location of wave breaking in this trial. These increased pressures contrast with load cell measurements showing a 20% reduction of force in the neighboring specimen, suggesting a potential for locally channelized flow inland of the mangroves leading to non-uniform pressures over the face of an inland structure. These differences may be owing to pressure gauges not extending to the crest of the structures and documented variability in impulsive pressure measurements (Witte, 1988; Oumeraci et al., 1993; Hattori et al., 1994). Pressure gauges have been shown to capture an impulsive spike due to wave breaking that is not necessarily registered by a load cell due to the inertia of the structure and short duration of the impulsive force (Bullock et al., 2007; Bradner et al., 2009). Additional work must further investigate the impulsive force associated with wave impact to determine outcomes for structures subject to short duration impacts followed by longer duration, quasi-static wave loading. A significant reduction in measured pressures for the shielded configurations is observed for ERF3C (Fig. A2(c)and(f)). This shorter time scale wave broke directly on the structure (near PG6) in the M0 configuration; the presence of mangroves caused wave energy dissipation offshore and significantly reduced the impulsive slamming force associated with the wave.

References

Alongi, D.M., 2008. Mangrove forests: resilience, protection from tsunamis, and responses to global climate change. Estuar. Coast Shelf Sci. 76 (1), 1–13. https://doi.org/10.1016/j.ecss.2007.08.024.

Anderson, M.E., Smith, J.M., 2014. Wave attenuation by flexible, idealized salt marsh vegetation. Coast. Eng. 83, 82–92.

Bao, T.Q., 2011. Effect of mangrove forest structures on wave attenuation in coastal Vietnam. Oceanologia 53 (3), 807–808.

Blackmar, P.J., Cox, D.T., Wu, W.C., 2014. Laboratory observations and numerical simulations of wave height attenuation in heterogeneous vegetation. J. Waterw. Port, Coast. Ocean Eng. 140 (1), 56–65.

Bradner, C., Schumacher, T., Cox, D., Higgins, C., 2009. Large scale laboratory measurements of wave forces on highway bridge superstructures. In: Proceedings of the 31st International Conference, pp. 3554–3566. Hamburg, Germany.

Bremm, G.C., Goseberg, N., Schlurmann, T., Nistor, I., 2015. Long wave flow interaction with a single square structure on a sloping beach. J. Mar. Sci. Eng. 3, 821–844. https://doi.org/10.3390/jmse3030821.

Bullock, G.N., Obhrai, C., Peregrine, D.H., Bredmose, H., 2007. Violent breaking wave impacts. Part 1: results from large-scale regular wave tests on vertical and sloping walls. Coast. Eng. 54, 602–617, 2007.

Chang, S.E., Adams, B.J., Alder, J., Berke, P.R., Chuenpagdee, R., Ghosh, S., Wabnitz, C., 2006. Coastal ecosystems and tsunami protection after the December 2004 Indian Ocean tsunami. Earthq. Spectra 22, S863eS887.

Chen, E.S., Melville, W.K., 1988. Deep-water plunging wave pressures on a vertical plane wall. Proc. Roy. Soc. Lond. A. 417, 95–131.

Cheong, S.M., Silliman, B., Wong, P.P., van Wesenbeeck, B., Guannel, G., 2013. Coastal adaptation with ecological engineering. Nat. Clim. Change. https://doi.org/10.1038/NCLIMATE1854.

Clough, B., Phillips, M., Xuan, T.T., 1999. Termination Report, PN 9412: Mixed Shrimp Farming Mangrove Forestry Models in the Mekong Delta. Australian Institute of Marine Science, p. 50.

Clough, B.F., Scott, K., 1989. Allometric relationships for estimating above-ground biomass in six mangrove species. For. Ecol. Manage. 27, 117–127.

Cooker, M.J., Peregrine, D.H., 1995. Pressure impulse theory for liquid impact problems. J. Fluid Mech. 297, 193–214.

Danielsen, F., Sørenson, M.K., Olwig, M.F., Selvam, V., Parish, F., Burgess, N.D., Hiraishi, T., Karunagaran, V.M., Rasmussen, M.S., Hansen, L.B., Quarto, A., Suryadiputra, N., 2005. The Asian Tsunami: A protective role for coastal vegetation. Science 310 (5748), 643. https://doi.org/10.1126/science.1118387.

Dawes, C., Siar, K., Marlett, D., 1999. Mangrove structure, litter, and macroalgal productivity in a northern-most forest of Florida. Mangroves Salt Marshes 3, 259–267.

Duke, N.C., Ball, M.C., Ellison, J.C., 1998. Factors influencing biodiversity and distributional gradients in mangroves. Global Ecol. Biogeogr. Lett. 7, 27–47.

Duke, N.C., Lo, E.Y.Y., Sun, M., 2001. Global distribution and genetic discontinuities of mangroves- emerging patterns in the evolution of *Rhizophora.* Trees (Berl.) 16, 65–79. https://doi.org/10.1007/s00468-001-0141-7, 2002.

Ellison, A.M., 2002. Macroecology of mangroves: large-scale patterns and processes in tropical coastal forests. Trees Struct. Funct. 16, 181–194.

Environmental Agency – Abu Dhabi, 2015. EAD-TMBS-TG-01: Technical Guidance Document for Mangrove Planting Permitting and Management Plan. Environmental Agency – Abu Dhabi, p. 44.

Farber, S., Costanza, R., Childers, D.L., Erickson, J., Gross, K., Grove, M., Hopkinson, C. S., Kahn, S., Pincetl, S., Troy, A., Warren, P., Wilson, M., 2006. Linking ecology and economics for ecosystem management. Bioscience 56 (2), 117–129.

Giri, C., Ochient, E., Tieszen, L.L., Zhu, Z., Singh, A., Loveland, T., Masek, J., Duke, N., 2011. Status and distribution of mangrove forests of the world using earth observation satellite data. Global Ecol. Biogeogr. 20, 154–159. https://doi.org/10.1111/j.1466-8238.2010.005864.x, 2011.

Goseberg, N., Wurpts, A., Schlurmann, T., 2013. Laboratory-scale generation of tsunami and long waves. Coast. Eng. 79 (2013), 57–74.

Guannel, G., Arkema, K., Ruggiero, P., Verutes, G., 2016. The power of three: coral reefs, seagrasses and mangroves protect coastal regions and increase their resilience. PloS One 11 (7), 22.

Hashim, A.M., Catherine, S.M.P., 2013. A laboratory study on wave reduction by mangrove forests. APCBEE Procedia 5 (2013), 27–32.

Hattori, M., Arami, A., Yui, T., 1994. Wave impact pressure on vertical walls under breaking waves of various types. Coast. Eng. 22 (1–2), 779-114.

Horstman, E.M., Dohmen-Janssen, C.M., Narra, P.M.F., van den Berg, N.J.F., Siemerink, M., Hulscher, S.J.M.H., 2014. Wave attenuation in mangroves: a quantitative approach to field observations. Coast. Eng. 94, 47–62, 2014.

Huang, Z., Yao, Y., Sim, S.Y., Yao, Y., 2011. Interaction of solitary waves with emergent, rigid vegetation. Ocean. Eng. 38, 1080–1088.

IPCC, 2013. In: Stocker, T.F., Qin, D., Plattner, G.-K., Tignor, M., Allen, S.K., Boschung, J., Nauels, A., Xia, Y., Bex, V., Midgley, P.M. (Eds.), Climate Change 2013: The Physical Science Basis. Contribution of Working Group I to the Fifth Assessment Report of the Intergovernmental Panel on Climate Change, 1. Cambridge University Press, Cambridge, United Kingdom and New York, NY, USA, p. 535.

Irish, J.L., Weiss, R., Yang, Y., Song, Y.K., Zainali, A., Marivela-Colmenarejo, R., 2014. Laboratory experiments of tsunami run-up and withdrawal in a patchy coastal forest on a steep beach. Nat. Hazards 74, 1933–1949.

Irtem, E., Gedik, N., Kabdasli, M.S., Yasa, N.E., 2009. Coastal forest effects on tsunami run-up heights. Ocean. Eng. 36, 313–320.

Ismail, H., Abd Wahab, A.K., Alias, N.E., 2012. Determination of mangrove forest performance in reducing tsunami run-up using physical models. Nat. Hazards 63, 939–963.

Ismail, I., Husain, M.L., Zakaria, R., 2017. Attenuation of waves from boat wakes in mixed mangrove forest of rhizophora and bruguiera species in Matang, Perak. Malaysian Journal geosciences 1 (2), 29–32, 2017.

Jin Eong, O., Khoon, G.W., Clough, B.F., 1995. Structure and productivity of a 20-year-old stand of Rhizophora apiculata Bl. mangrove forest. J. Biogeogr. 22, 417–424.

Kamiyama, A., Moriya, H., Prawiroatmodojo, S., Toma, T., Ogino, K., 1988. Biological system of mangroves: A report of east Indonesian mangrove expedition. In: Oginao, K., Chihara, M. (Eds.), Forest Primary Productivity, 2. Ehime University, Japan, pp. 97–117, 1986.

Kathiresan, K., Rajendran, N., 2005. Coastal mangrove forests mitigated tsunami. Estuar. Coast Shelf Sci. 65, 601–606, 2005.

Kazemi, A., van de Riet, K., Curet, O.M., 2018. Drag coefficient and flow structure downstream of mangrove root-type models through PIV and direct force measurements. Physical Review Fluids 3, 20, 073801.

Krauss, K., Doyle, T., Doyle, T., Swarzenski, C., From, A., Day, R., Conner, W., 2009. Water level observations in mangrove swamps during two hurricanes in Florida. Wetlands 29, 142–149.

Lara, J.L., Maza, M., Ondiviela, B., Trinogga, J., Losada, I.J., Bouma, T.J., Gordejuela, N., 2016. Large-scale 3-D experiments of wave and current interaction with real vegetation. Part 1: Guidelines for physical modeling. Coast. Eng. 107, 70–83.

Liu, H., Zhang, K., Li, Y., Xie, L., 2013. Numerical study of the sensitivity of mangroves in reducing storm surge and flooding to hurricane characteristics in southern Florida. Continent. Shelf Res. 64, 51–65, 2013.

Liu, P.L.-F., Cheng, C.W., Mei, C.C., Lomonaco, P., Martin, F.L., Maza, M., 2015. Periodic Waves through an aquatic forest. Coast. Eng. 96, 100–117. https://doi.org/10.1016/j.coastaleng.2014.11.002, 2015.

Lovelock, C.E., Kraus, K., Osland, M.J., Reef, R., Ball, M.C., 2019. The physiology of mangrove trees with changing climate. In: Goldstein, G.H., Santiago, L.S. (Eds.), Tropical Tree Physiology: Adaptations and Responses in a Changing Environment. Springer, New York, New York.

Madsen, P.A., Fuhrman, D.R., Schaffer, H.A., 2008. On the solitary wave paradigm for tsunamis. J. Geophys. Res. 113, C12012. https://doi.org/10.1029/2008JC004932.

Maza, M., Lara, J.L., Losada, I.J., Ondiviela, B., Trinogga, J., Bouma, T.J., 2015a. Large-scale 3-D experiments of wave and current interaction with real vegetation. Part 2: Experimental analysis. Coast. Eng. 106, 73–86, 2015.

Maza, M., Lara, J.L., Losada, I.J., 2015b. Tsunami wave interaction with mangrove forests: A 3 D Numerical approach. Coast. Eng. 98 (2015), 33–54.

Maza, M., Lara, J.L., Losada, I.J., 2016. Solitary wave attenuation by vegetation patches. Adv. Water Resour. 98, 159–172, 2016.

Maza, M., Adler, K., Ramos, D., Garcia, A.M., Nepf, H., 2017. Velocity and Drag Evolution from the leading edge of a model mangrove forest. J. Geophys. Res. B: Oceans 122, 16. https://doi.org/10.1002/2017JC012945.

Maza, M., Lara, J.L., Losada, I.J., 2019. Experimental analysis of wave attenuation and drag forces in a realistic fringe *Rhizophora* mangrove forest. Adv. Water Resour. 131, 103376, 2019.

Mazda, Y., Magi, M., Kogo, M., Hong, P.N., 1997a. Mangroves as a coastal protection from waves in the tong king delta, vietnam, mangr. Salt Marsh 1 (2), 127–135. https://doi.org/10.1023/A:1009928003700.

Mazda, Y., Wolanski, E.J., King, B.A., Sase, A., Ohtsuka, D., Magi, M., 1997b. Drag force due to vegetation in mangrove swamps. Mangroves Salt Marshes 1, 193–199, 1997.

Mendez, F.J., Losada, I.J., 2004. An empirical model to estimate the propagation of random breaking and non-breaking waves over vegetation fields. Coast. Eng. 52, 103–118.

Narayan, S., Beck, M.W., Reguero, B.G., Losada, I.J., van Wesenbeeck, B., Pontee, N., Sanchirico, J.N., Ingram, J.C., Lange, G.M., Burks-Copes, K.A., 2016. The effectiveness, costs, and coastal protection benefits of natural and nature-based defences. PLoS One 11 (5), 17.

Nepf, H., 1999. Drag, turbulence, and diffusion in flow through emergent vegetation. Water Resour. Res. 35 (2), 479–489.

Nepf, H., 2004. Vegetative flow dynamics. In the ecogeomorphology of tidal marshes. Coast. Estuar. Stud. 59, 137–163.

Nepf, H., Vivoni, E.R., 2000. Flow structure in depth-limited, vegetated flow. J. Geophys. Res.: Oceans 105, C12. https://doi.org/10.1029/2000JC900145.

Neumeier, U., 2007. Velocity and turbulence variations at the edge of saltmarshes. Continent. Shelf Res. 27, 1046–1059. https://doi.org/10.1016/j.csr.2005.07.009.

Novitzky, P., 2010. Analysis of Mangrove Structure and Latitudinal Relationships on the Gulf Coast of Peninsular Florida. University of South Florida.

Ohira, W., Honda, K., Nagai, M., Ratanasuwan, A., 2013. Mangrove stilt root morphology modelling for estimating hydraulic drag in tsunami inundation simulation. Trees (Berl.) 27, 141–148.

Ong, J.E., Gong, W.K., Wong, C.H., 2004. Allometry and partitioning of the mangrove, *Rhizophora apiculata*. For. Ecol. Manag. 188, 395–408, 2004.

Oumeraci, H., Klammer, P., Partenscky, H.W., 1993. Classification of breaking wave loads on vertical structures. J. Waterw. Port, Coast. Ocean Eng. 119 (4), 381–397.

Ozeren, Y., Wren, D.G., Wu, W., 2014. Experimental investigation of wave attenuation through model and live vegetation. J. Waterw. Port, Coast. Ocean Eng. 140 (5), 04014019.

Park, H., Tomiczek, T., Cox, D.T., van de Lindt, J.W., Lomonaco, P., 2017. Experimental modeling of horizontal and vertical wave forces on an elevated coastal structure. Coast. Eng. 128, 58–74, 2017.

Peregrine, D.H., 2003. Water wave impacts on walls. Annu. Rev. Fluid Mech. 35, 23–43.

Pontee, N.I., Narayan, S., Beck, M., Hosking, A.H., 2016. Building with nature: Lessons from around the world. Maritime Engineering Journal 169 (1), 29–36.

Prasetyo, A., Yasuda, T., Miyashita, T., Mori, N., 2019. Physical modeling and numerical analysis of tsunami inundation in a coastal city. Front. Built. Environ. 5, 46. https://doi.org/10.3389/fbuil.2019.00046.

Quartel, S., Kroon, A., Augustinus, P., van Santen, P., Tri, N.H., 2007. Wave attenuation in coastal mangroves in the red river delta, vietnam. J. Asian Earth Sci. 29 (4), 576–584. https://doi.org/10.1016/j.jseaes.2006.05.008.

Quisthoudt, K., Schmitz, N., Randin, C.F., Dahdouh-Guebas, F., Robert, E.M.R., Koedam, N., 2012. Temperature variation among mangrove latitudinal range limits worldwide. Trees (Berl.) 26, 1919–1931. https://doi.org/10.1007/s00468-012-0760-1, 2012.

Reid, W.V., Mooney, H.A., Cropper, A., Capistrano, D., Carpenter, S.R., Chopra, K., Dasgupta, P., Dietz, T., Duralappah, A.K., Hassan, R., Kasperson, R., Leemans, R., May, R.M., McMichael, T., Pingali, P., Samper, C., Scholes, R., Watson, R.T., Zakri, A. H., Shidong, Z., Ash, N.J., Bennett, E., Kumar, P., Lee, M.J., Raudsepp-Hearne, R., Simons, H., Thonell, J., Zurek, M.B., 2005. Ecosystems and Human Well-Being: Synthesis. *Millennium Ecosystem Assessment*. Island Press, Washington, D.C.

Rominger, J.T., Nepf, H.M., 2014. Effects of blade flexural rigidity on drag force and mass transfer rates in model blades. Limnol. Oceanogr. 59 (6), 2028–2041. https://doi.org/10.4319/lo.2014.59.6.2028.

Rossetto, T., Allsop, W., Charvet, I., Robinson, D.I., 2011. Physical modelling of tsunami using a new pneumatic wave generator. Coast. Eng. 58 (6), 517–527.

Scyphers, S.B., Powers, S.P., Heck, K.L., Byron, D., 2011. Oyster reefs as natural breakwaters mitigate shoreline loss and facilitate fisheries. PloS One 6 (8). https://doi.org/10.1371/journal.pone.0022396.

Scyphers, S.B., Picou, J.S., Powers, S.P., 2015. Participatory conservation of coastal habitats: the importance of understanding homeowner decision making to mitigate cascading shoreline degradation. Conservation Letters 8 (1), 41–49.

Sheng, Y.P., Zou, R., 2017. Assessing the role of mangrove forest in reducing coastal inundation during major hurricanes. Hydrobiologia 803, 87–103. https://doi.org/10.1007/s10750-017-3201-8, 2017.

Small, C., Nicholls, R.J., 2003. A global analysis of human settlement in coastal zones. J. Coast Res. 19 (3), 584–599.

Smith, J.M., Anderson, M., 2014. Limits of wetland wave dissipation. Coastal Eng. Proceedings 34, 9. https://doi.org/10.9753/icce.v34.waves.18, 2014. Seoul, Korea.

Spalding, M.D., Blasco, F., Field, C.D., 1997. World Mangrove Atlas. International Society for Mangrove Ecosystems, Okinawa, Japan.

Spalding, M.D., Kainuma, M., Collins, L., 2010. World Atlas of Mangroves, 319. Earthscan, London.

Sreelekshmi, S., Preethy, C.M., Varghese, R., Joseph, P., Asha, C.V., Nandan, S.B., Radhakrishnan, C.K., 2018. Diversity, stand structure, and zonation pattern of mangroves in southwest coast of India. J. Asia-Pacific Biodiversity 11 (4), 573–582. https://doi.org/10.1016/j.japb.2018.08.001.

Strusińska-Correia, A., Husrin, S., Oumeraci, H., 2013. Tsunami damping by mangrove forest: a laboratory study using parameterized trees. Nat. Hazards Earth Syst. Sci. 13, 483–503. https://doi.org/10.5194/nhess-13-483-2013.

Sweet, W.V., Kopp, R.E., Weaver, C.P., Obeysekera, J., Horton, R.M., Thieler, E.R., Zervas, C., 2017. Global and Regional Sea Level Rise Scenarios for the United States. NOAA Tech. Rep. NOS CO-OPS 083. National Oceanic and Atmospheric Administration. National Ocean Service, Silver Spring, MD, p. 75, 28 February 2019. https://tidesandcurrents.noaa.gov/publications/techrpt83_Global_and_Regional_SLR_Scenarios_for_the_US_final.pdf.

Synolakis, C., 1990. Generation of long waves in laboratory. J. Waterw. Port, Coast. Ocean Eng. 116 (2), 252–266.

Tamai, S., Nakasuga, T., Tabuchi, R., Ogino, K., 1983. Ecological studies of mangrove forests in southern Thailand—standing structure and biomass. In: Mangrove Ecology in Thailand, Thai—Japanese Cooperative Research Project on Mangrove Productivity and Development. Japanese Ministry of Education, Science, and Culture, pp. 3–15, 1981-1982.

Tanino, Y., Nepf, H., 2008. Laboratory investigation on mean drag in a random array of rigid, emergent cylinders. J. Hydraul. Eng. 134, 34–41.

Thomas, S., Cox, D., 2012. Influence of finite-length seawalls for tsunami loading on coastal structures. J. Waterw. Port, Coast. Ocean Eng. 138 (3), 203–214.

Thuy, N.B., Nandasena, N.A.K., Dang, V.H., Kim, S., Hien, N.X., Hole, L.R., Thai, T.H., 2017. Effect of river vegetation with timber piling on ship wave attenuation: investigation by field survey and numerical modeling. Ocean. Eng. 129, 37–45, 2017.

Tomiczek, T., Prasetyo, A., Mori, N., Yasuda, T., Kennedy, A., 2016. Physical modelling of tsunami onshore propagation, peak pressures, and shielding effects in an urban array. Coast. Eng. 117, 97–112, 2016.

Tomiczek, T., O'Donnell, K., Furman, K., Webbmartin, B., Scyphers, S., 2020. Rapid damage assessments of shorelines and structures in the Florida Keys after hurricane Irma. Nat. Hazards Rev. 21 (1) https://doi.org/10.1061/(ASCE)NH.1527-6996.0000349.

Tomiczek, T., Wargula, A., Jendrysik, M., Goodwin, S., Kennedy, A.B., Lynett, P., Lomonaco, P., Cox, D.T., 2019. Physical Model Investigation of Parcel-Scale Effects of Mangroves on Wave Transformation and Force Reduction in the Built Environment. In: Coastal Structures Proceedings, September 28-October 2, 2019. ASCE, Hannover, Germany, pp. 1–10.

Trung, V.L., Yagisawa, J., Tanaka, N., 2015. Efficacy of *Rhizophora apiculata* and *Nypa Fruticans* on attenuation of boat-generated waves under steep slope condition. Int. J. Ocean Water Resour. 19 (2), 1103–1114.

Witte, H.H., 1988. Wave induced impact loading in deterministic and stochastic reflection. Mittl. - Leichtweiss Inst. Wasserbau Tech. Univ. Braunschw. 102, 1–227.

Wood, D.J., Peregrine, D.H., Bruce, T., 2000. Wave impact on a wall using pressure-impulse theory. I: trapped air. J. Waterw. Port, Coast. Ocean Eng. 126 (4), 182–190.

Wu, W.C., Cox, D.T., 2015a. Effects of vertical variation in vegetation density on wave attenuation. J. Waterw. Port, Coast. Ocean Eng. 142, 2.

Wu, W.C., Cox, D.T., 2015b. Effects of wave steepness and relative water depth on wave attenuation by emergent vegetation, Estuarine. Coastal and Shelf Science 164, 443–450.

Wu, W.C., Ma, G., Cox, D.T., 2016. Modeling wave attenuation induced by the vertical density variations of vegetation. Coast. Eng. 112, 17–27, 2016.

Yanagisawa, H.K.S., Goto, K., Miyagi, T., Imamura, F., Ruangrassamee, A., Tanavud, C., 2009. The reduction effects of mangrove forest on a tsunami based on field surveys at Pakarang Cape, Thailand and numerical analysis. Estuar. Coast Shelf Sci. 81, 27–37.

Zhang, K., Liu, H., Li, Y., Xu, H., Shen, J., Rhome, J., Smith III, T.J., 2012. The role of mangroves in attenuating storm surges. Estuar. Coast Shelf Sci. 102–103, 11–23, 2012.

Zhang, X., Chua, V.P., Cheong, H.F., 2015. Hydrodynamics in mangrove prop roots and their physical properties. Journal of Hydro-Environment Research 9, 281–294.